Paleoceanography and Paleoclimatology

RESEARCH ARTICLE
10.1029/2025PA005304

Enhanced Last Glacial Aridity in the Western Pampean Plains Inferred From Southern South American Loess

Diego A. Montecino Jara[1,2], Victoria Nogués[1,2], Nicolás J. Cosentino[3,4,5], Gabriela Torre[1,2], Renata Coppo[6], André O. Sawakuchi[7], Ana Laura Berman[3,4,5], and Diego M. Gaiero[1,2]

[1]CICTERRA, UNC-CONICET, Córdoba, Argentina, [2]Facultad de Ciencias Exactas, Físicas y Naturales, Universidad Nacional de Córdoba, Córdoba, Argentina, [3]Facultad de Ciencias Exactas y Naturales, Universidad de Buenos Aires, Buenos Aires, Argentina, [4]Centro de Investigaciones del Mar y la Atmósfera (CIMA), CONICET-UBA, Buenos Aires, Argentina, [5]Instituto Franco-Argentino de Estudios sobre el Clima y sus Impactos (IFAECI, IRL 3351), CNRS-CONICET-IRD-UBA, Buenos Aires, Argentina, [6]Istituto di Scienze dell'Atmosfera e del Clima, Consiglio Nazionale delle Ricerche, Turin, Italy, [7]Luminescence and Gamma Spectrometry Laboratory (LEGaL), Institute of Geosciencies, University of São Paulo, São Paulo, Brazil

Key Points:

- Reconstructed 43,000 years of dust activity in southern South America from a loess record in the Pampean plains
- During the Last Glacial Maximum, wetter sources and arid Pampean plains sharply reduced dust deposition
- Deglaciation and Holocene dust deposition were driven by stronger winds, dry source regions, and wetter sink region

Supporting Information:

Supporting Information may be found in the online version of this article.

Correspondence to:

D. A. Montecino Jara and D. M. Gaiero,
diego.montecino@mi.unc.edu.ar;
diego.gaiero@unc.edu.ar

Citation:

Montecino Jara, D. A., Nogués, V., Cosentino, N. J., Torre, G., Coppo, R., Sawakuchi, A. O., et al. (2026). Enhanced Last Glacial aridity in the western Pampean plains inferred from southern South American loess. *Paleoceanography and Paleoclimatology*, *41*, e2025PA005304. https://doi.org/10.1029/2025PA005304

Received 19 AUG 2025
Accepted 24 JAN 2026

Abstract Understanding why proximal loess in southern South America (SSA) exhibits a contrasting evolution of dust deposition flux since the Last Glacial Maximum (LGM) compared to that of distal Southern Hemisphere (SH) archives remains a major unresolved problem. To shed light on this issue, this study examines dust emission, transport, and deposition in SSA over the past 43,000 years through multiproxy analysis of a Pampean loess section. We reconstruct dust mass accumulation rates (DMAR) and their controls through quartz and feldspar luminescence dating, sediment properties, and paleoclimate simulations. Increased DMAR was observed during Marine Isotope Stage 3 due to greater sediment availability and humid conditions. A sharp decline during the LGM was linked to wetter source areas and arid Pampean conditions that reduced wet dust deposition efficiency, while intensified Southern Westerly Winds strengthened dust emissions from proximal sources, as well as dry coarse dust deposition at the study site. During deglaciation, dust deposition in the Pampean region occurred under windier but relatively wetter conditions, resulting in dry sedimentation dominated by coarser fractions from nearby sources. In the Holocene, DMAR reflects the combined effects of enhanced dust emission under arid conditions in source regions and increasing precipitation after ~3.9 ka in the Pampean plains. Our results provide constraints on accumulation modes and sediment provenance, showing how hydroclimate variability and sediment availability shaped SSA dust dynamics. Together, they reconcile contrasting dust flux trends between proximal Pampean loess and distal SH archives through coupled changes in source activity, depositional processes, and atmospheric circulation.

Plain Language Summary Over the past 43,000 years, strong winds have moved vast amounts of dust across southern South America, yet when, where, and why this happened is not fully clear. We examined a thick deposit of windblown sediments, known as loess, in the Pampean plains of Argentina to see how dust production and deposition have changed through time. Using dating methods, sediment analyses, and climate model simulations, we reconstructed dust accumulation rates and traced their sources. Dust levels increased when source regions were dry and winds could lift abundant loose material. They dropped sharply during the coldest part of the last ice age, when sources became wetter and the Pampean plains were drier, reducing deposition. As the climate warmed, dry nearby sources, and stronger winds brought coarser dust. In recent millennia, dry sources, and wetter conditions in the Pampean plains together shaped how much dust was deposited.

1. Introduction

Atmospheric circulation is fundamental to Earth's climate, redistributing heat and moisture and transporting windblown dust across the planet. Dust deposits, such as loess, are a valuable geological archive that record past atmospheric and environmental variability, including changes in latitudinal position and intensity of major wind belts, aridity and sediment availability, in response to climatic changes (Kohfeld & Harrison, 2001; Lambert et al., 2008). These variations are particularly pronounced during glacial-interglacial transitions, which mark major shifts in global dust activity (Simonsen et al., 2019). Dust emission is generally enhanced under conditions of strong winds, reduced soil moisture, and limited vegetation cover (Csavina et al., 2014; Munson et al., 2011), while dust deposition and loess formation are strongly controlled by precipitation patterns (Pye & Tsoar, 1987).

Southern South America (SSA) is one of the Southern Hemisphere (SH)'s most important dust-producing regions, supplying mineral aerosols to both the South Atlantic Ocean and the East Antarctic Plateau during glacial and interglacial periods (Delmonte et al., 2004, 2010; Gaiero et al., 2007; Grousset et al., 1992). The strong rain shadow of the Andes sustains the South American Arid Diagonal (SAAD; Blisniuk et al., 2005), an extensive north–south belt of arid and semi-arid environments that hosts the main past and present dust sources: the Puna–Altiplano Plateau (PAP, ∼15–28°S), central-western Argentina (CWA, ∼27–36°S), and eastern Patagonia (∼37–54°S; Figure 1). Dust emission in these regions is primarily controlled by wind strength, sediment availability, and soil moisture (Bullard et al., 2011; Kok et al., 2012; Shao, 2008), with sustained activity requiring both strong winds and abundant fine-grained material (Bullard et al., 2011; Prospero et al., 2002).

Atmospheric circulation over SSA regulates both hydroclimate and dust transport pathways. During austral summer, precipitation patterns are dominated by the South American Summer Monsoon System and the South American Low-Level Jet, which transport Amazonian moisture south toward the subtropical plains east of the SAAD (Bruniard, 1982; Garreaud et al., 2009; Piovano et al., 2009; Vera et al., 2006). In austral winter, the Subtropical Jet (STJ, ∼15–60°S) intensifies at high altitude, while the low-altitude, sub-polar Southern Westerly Winds (SWW, ∼30–65°S) transport Pacific moisture to western SSA, becoming dry after crossing the Andes (Garreaud et al., 2009). Together, these zonal systems exert primary control on the mobilization, uplift, and transport of dust from the main SSA sources.

Within the SAAD, dust sources reflect contrasting geomorphological and atmospheric contexts. In the PAP, winter strengthening of the STJ favors the entrainment of dust into the upper troposphere, enabling long-distance transport (Gaiero et al., 2013; Koch et al., 2006). Key deflation surfaces include saline lakes, remnants of large late Pleistocene lake systems, alluvial fans, evaporite playas, and extensive aeolian deposits (Martin et al., 2018; McMillan & Schoenbohm, 2020; Milana, 2009; Milana et al., 2010, 2011; Placzek et al., 2006, 2013). In southern CWA (SCWA, 32–36°S), hot and dry Zonda winds, katabatic flows occurring mainly from May to August, inject dust into the troposphere, where it is subsequently transported by the STJ and other upper-level jets (Mingari et al., 2017; Norte et al., 2008). Sediment sources include fluvial and alluvial systems between the Andes and the Sierras de San Luis, Comechingones, and Córdoba, with the Bermejo–Desaguadero–Salado system supplying much of the silt-sized material (Prospero et al., 2002; Schaetzl et al., 2018). Patagonia constitutes another major dust-producing region due to the combination of persistent SWW, high aridity, and widespread fine-grained deposits. Major sources include glacial, glaciofluvial, lacustrine, and volcanic sediments located in outwash plains and ephemeral lake basins between the Andes and the Atlantic coast (Gassó et al., 2010; Ginoux et al., 2012; Prospero et al., 2002; Villarreal & Coronato, 2017), with seasonal dust maxima in spring–summer (Cosentino et al., 2020, 2021).

East of the SAAD, the Pampean loess forms the largest loess deposit in the SH, covering ∼600,000 km^2 with thicknesses up to ∼50 m (Figure 1). This region has acted as a proximal dust sink since the Miocene (Iriondo & Kröhling, 2007; Stubbins et al., 2023; Zárate, 2003). Loess deposits preserve past atmospheric circulation patterns and record dust mass accumulation rates (DMAR) that reflect hydroclimatic variability such as changes in precipitation frequency and drought intensity (Marx et al., 2018). The Last Glacial Maximum (LGM; 26.5–19.0 ka; Clark et al., 2009) was characterized by increased dust fluxes in both the South Atlantic Ocean and East Antarctic Plateau (Lambert et al., 2008; Petit et al., 1990). In contrast, the Pampean loess exhibits its lowest DMAR values during the same interval (Coppo et al., 2022). These contrasting proximal versus intermediate/distal trends remain unresolved, with hypotheses invoking changes in transport efficiency, shifts in dust source activity, or altered precipitation regimes affecting wet scavenging (Coppo et al., 2022; Lambert et al., 2008; Petit & Delmonte, 2009; Torre et al., 2022).

Despite progress in identifying the main dust sources and transport pathways in SSA, critical knowledge gaps persist regarding the mechanisms controlling dust fluxes during late Quaternary climate transitions. Four key uncertainties require further research: (a) how glacial–interglacial transitions change the position and intensity of the STJ, SWW, and Zonda winds influencing dust mobilization and transport (Kohfeld et al., 2013; Moreno et al., 2018; Quade & Kaplan, 2017; Rojas, 2013); (b) the potential for higher SWW transport efficiency during cold periods (LGM, Antarctic Cold Reversal: ACR), possibly linked to strengthened Zonda winds activating SCWA/northern Patagonian sources; (c) the role of increased El Niño-like conditions during warm periods (Holocene) in enhancing sediment deflation from a drier PAP and deposition over the humid Pampas (Torre et al., 2022); and (d) the possibility that minimum Pampean loess DMARs during the LGM resulted from reduced

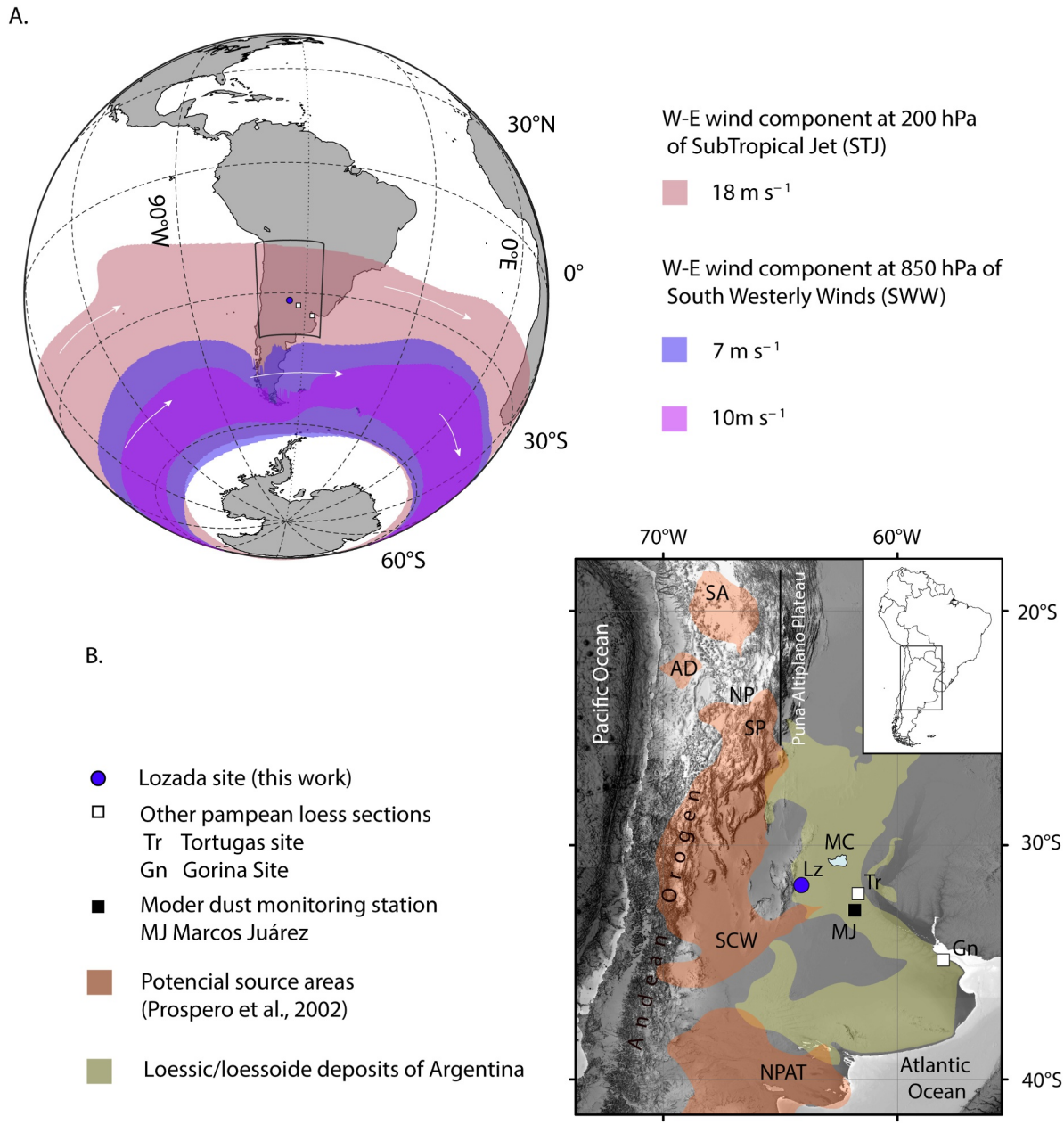

Figure 1. (a) Distribution of dust records alongside key Southern Hemisphere wind systems. Blue-purple shaded areas indicate regions where the west-east wind component at 850 hPa exceeds 7 and 10 m s^{-1}, reflecting the influence of the Southern Westerly Winds, while the reddish zone marks the Subtropical Jet, defined by the 18 m s^{-1} contour at 200 hPa. Wind patterns are based on 1979–2020 ERA5 climatological averages, with white arrows showing prevailing directions. (b) Locations of loess profiles: Lozada (blue dot), Tortugas and Gorina (white squares), and the Marcos Juárez station (black square). The yellow area marks loess deposits in the Chaco-Pampean plains (Zárate, 2003), while orange regions highlight major dust source areas in southern South America (Prospero et al., 2002), including the Puna-Altiplano Plateau (PAP), Southern Altiplano (SA), Northern Puna (NP), and Southern Puna (SN), Atacama Desert (AD), Southern Central-West Argentina (SCW), Mar Chiquita lake (MC), and Northern Patagonia (N-Pat).

wet scavenging of fine-grained dust particles in the region, potentially linked to lower precipitation frequency and intensity in the Pampas (Coppo et al., 2022) and/or limited sediment availability in dust-producing regions.

To address these uncertainties, we analyze the Lozada loess profile in the western Pampean region (Figure 1). Using a multiproxy approach, we (a) reconstruct DMAR variability from Marine Isotope Stage 3 (MIS 3) to the Late Holocene; (b) evaluate how atmospheric circulation and environmental conditions in the PAP, SCWA, and Patagonian sources influenced dust emission and transport; and (c) assess how hydroclimatic conditions along the

transport path and at the accumulation site modulated dust deposition. This framework provides new constraints on long-term SSA dust routing and the climatic drivers shaping contrasting dust fluxes across the SH.

2. Materials and Methods

2.1. Sediment Sampling

We sampled a vertical loess section (Lozada: 31.64983°S, 64.13461°W) exposed along an abandoned road excavation on an extensive alluvial plain, over the foothills of the eastern Pampean Ranges (Figure 1; Kemp et al., 2006). This site is located on the western fringes of the Pampean loess belt (e.g., Iriondo & Kröhling, 2007). Here, we complemented previous sampling in this site between 1.8 and 3.8 m below the surface (mbs; Coppo et al., 2022; Torre et al., 2019), with new sampling between 0.4–1.8 and 3.8–4.8 mbs. See details on sampling procedure in Text S1 in Supporting Information S1.

2.2. Sediment Physical and Chemical Characterization

2.2.1. Magnetic Susceptibility

The low-frequency (χ_{LF}) and high-frequency (χ_{HF}) volumetric magnetic susceptibility (MS) of each sample were measured using a Bartington MS2B sensor. Samples were dried, weighed, and stored in 10-cm^3 polyethylene containers prior to measurements.

The values of χ_{LF} and χ_{HF} were obtained using frequencies of 0.465 kHz ± 1% (κ_{LF}) and 4.65 kHz ± 1% (κ_{HF}), respectively. Three readings were taken per sample, alternating with a blank (i.e., air) reading used as a correction factor. Both χ_{LF} and χ_{HF} were calculated by normalizing by the weight of each sample. Measurement reproducibility was tested using a standard sample (ferrite type B2; SI = 3,064 × 10^{-5}).

2.2.2. Organic Matter and Carbonate Contents

Approximately 1 g of each sample was placed in ceramic crucibles and processed in an electric furnace following the loss-on-ignition (LOI) method described by Heiri et al. (2001). To remove interstitial moisture, samples were first heated to 105°C. The loss on ignition at 550°C (LOI_{550}) was calculated in weight percent (wt.%) based on the difference between the dry weight and the weight after 4 hr of incineration at 550°C. Following Meyers & Lallier-Vergès (1999), total organic carbon (TOC) was estimated as half of the LOI_{550} value. Organic matter (OM) content was then calculated by multiplying TOC by 1.724 (van Bemmelen factor), which assumes that soil OM contains approximately 58% carbon (Howard & Howard, 1990).

A second incineration step was performed at 950°C for 2 hr to remove carbonate minerals. Total inorganic carbon (TIC) was estimated based on the assumption that carbonate decomposition follows a stoichiometric reaction (Heiri et al., 2001). In most sediments, carbonates are the main source of inorganic carbon; therefore, carbonate content is directly related to TIC, representing the amount of inorganic carbon originally bound within carbonate minerals. According to this method, carbonate content can be calculated by multiplying the percentage weight loss at 950°C (LOI_{950}) by a factor of 1.36. This factor is derived from the molecular weights of carbon dioxide (44 g mol^{-1}) and carbonate (60 g mol^{-1}), assuming that the observed weight loss at 950°C corresponds entirely to CO_2 released from carbonate decomposition.

2.2.3. Grain Size

Grain size of collected samples was determined by laser diffraction with a Horiba LA-950 analyzer. Prior to this, carbonates were removed, and clay particles were dispersed to avoid post-sampling clay flocculation. See details on these sample preparation steps in Text S2 in Supporting Information S1.

Measurements were done by triplicate. Reproducibility of the measurements was tested using mixtures of glass beads as standards (NIST Traceable polydisperse particle standards PS202/3–30 μm and PS215/10-100 μm, Whitehouse Scientific).

2.3. Grain Size End-Member Analysis

Since the grain size distributions of the samples were generally multimodal, we conducted a statistical end-member analysis (EMA) using the AnalySize v1.2.2 algorithm (Paterson & Heslop, 2015). This approach decomposes the measured grain size distributions into a finite set of end members (EMs), each of which we interpreted in terms of specific sedimentary processes (Dietze et al., 2022).

2.4. Luminescence Dating

Luminescence dating laboratory work was carried out at the Luminescence and Gamma Spectrometry Laboratory (LEGAL) of the Institute of Geosciences of the University of São Paulo, Brazil.

Luminescence dating was performed using quartz optically stimulated luminescence (OSL) and K-feldspar post-infrared infrared stimulated luminescence (pIRIR) signal. Sample tubes were opened under subdued amber light. The sediment contained at the ends of the tube was set aside for dose rate measurements. The inner portion of the sediment was wet-sieved to separate the silt (<63 μm) and sand (63–250 μm) fractions. The sand fraction was further treated to isolate quartz and K-feldspar grains following procedures described in Text S3 in Supporting Information S1.

Two Risø TL/OSL DA-20 readers equipped with blue (470 nm) and infrared (830 nm) LEDs and $^{90}Sr/^{90}Y$ beta radiation sources with a dose rate of 0.12 and 0.088 Gy s^{-1} were used for luminescence measurements.

For quartz, the single-aliquot regenerative dose (SAR) protocol (Table S1 in Supporting Information S1; Murray & Wintle, 2003) was applied for equivalent dose (De) determinations. The De values for K-feldspar grains were determined using the post-infrared stimulated luminescence signal measured at 290°C ($pIRIR_{290}$), following Buylaert et al. (2012) and also described in Table S1 in Supporting Information S1. The $pIRIR_{290}$ method was selected because the De values of some samples were expected to exceed the saturation limit (~150 Gy) of quartz OSL. Dose rates were calculated based on the concentrations of ^{238}U, ^{232}Th, and ^{40}K determined by high-resolution gamma-ray spectrometry and conversion factors by Guérin et al. (2011). The cosmic radiation contribution to dose rate was calculated using the model by Prescott and Hutton (1994). More details on procedures and protocols for De and dose rate determinations can be found in Text S3 in Supporting Information S1.

2.5. Age-Depth Model

The Bayesian age-depth model was constructed using the Bacon package (Blaauw & Christen, 2011). The studied section was divided into 5-cm-thick segments, and the average accumulation rate suggested by the model (100 yr cm^{-1}) was applied. Bacon employs a Bayesian approach to model age-depth relationships in sedimentary sequences and is particularly robust against outliers, as it models them using a Student's *t*-distribution with wide tails. This allows ages that deviate significantly from the general trend to be managed without substantially affecting the final model (Blaauw & Christen, 2011).

A total of 23 ages were used to derive the age-depth model, estimated using three different OSL dating protocols. Thirteen of these ages were obtained in this study, and 10 were published previously (Coppo et al., 2022; Torre et al., 2019). Of these ages, 11 were obtained using the $pIRIR_{290}$ protocol on sand-sized K-feldspar grains, seven were determined using the SAR-OSL protocol on sand-sized quartz grains, and five were derived from silt-sized quartz grains measured using the post-IRSL OSL (pIRSL-OSL)protocol (Figure 2).

This approach allowed us to produce a consistent age-depth model that: (a) resolved two apparent age inversions by integrating stratigraphic order constraints, (b) provided a single age for two depths (i.e., 2.8 and 3.8 mbs), each of which were independently dated using different luminescence dating protocols, (c) provided a chronological framework to interpret the variability in physical and chemical parameters of the loess profile, and (d) allowed us to quantify the evolution of DMAR.

2.6. Definition of Stratigraphic Units

Stratigraphic units were defined by integrating field observations with laboratory analyses. In the field, we identified gradual color changes, from darker, pedogenically altered horizons to lighter, primary loess, along with key diagnostic features such as carbonate nodule, bioturbation, and locally preserved sub-horizontal lamination. This macroscopic framework was quantified and refined using systematic variability in measured parameters:

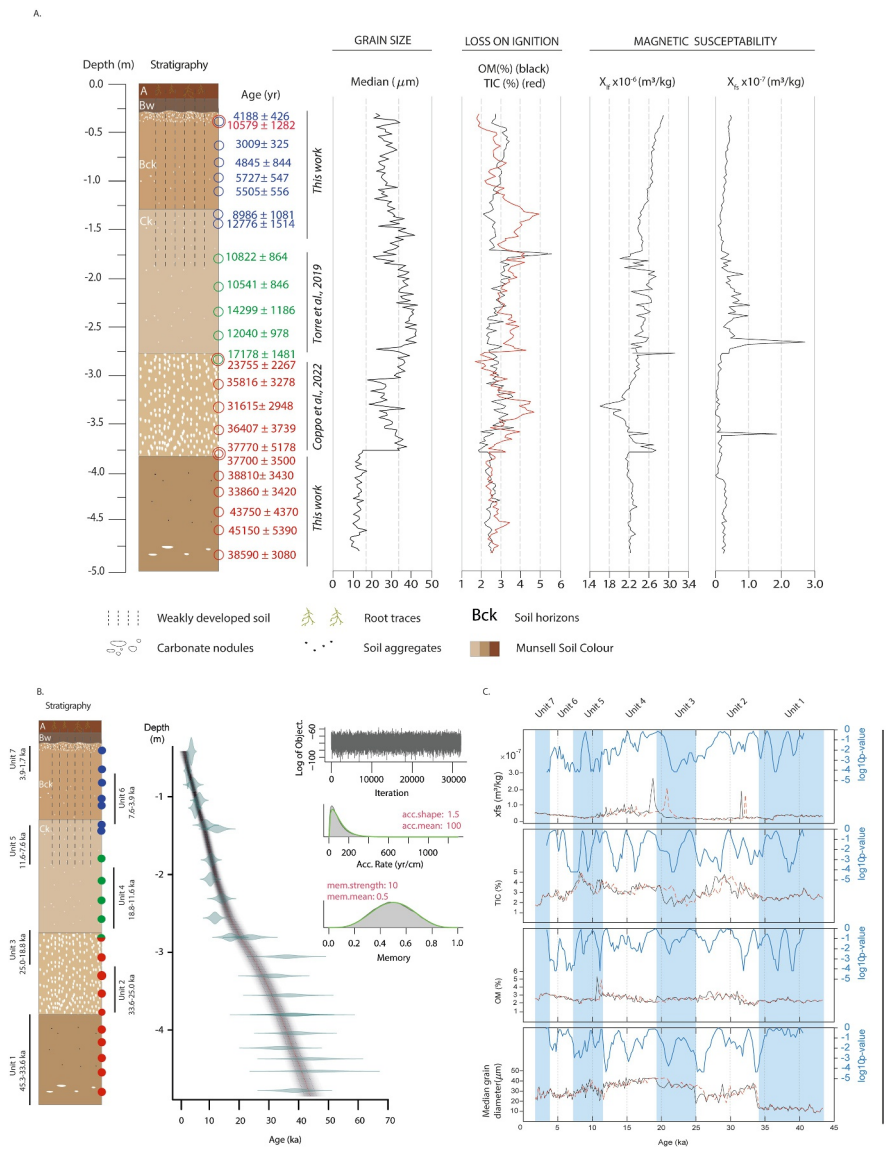

Figure 2. (a) Stratigraphic record of the Lozada section, including measured physical and chemical parameters, and ages. The age markers are color-coded by luminescence dating protocol: blue for quartz optically stimulated luminescence (OSL), green for quartz post-IRSL OSL, and red for K-feldspar $pIRIR_{290}$. (b) Age–depth model for the Lozada section alongside the stratigraphic units defined in this study. Green polygons depict the probability distributions of luminescence ages, with a gray shaded area marking the 68% confidence intervals from the Bayesian model. The central age estimates are shown by a red line. (c) Mann–Whitney tests applied to median grain size, organic matter, total inorganic carbon (TIC), and χ_{FS}. Depth intervals with significant changes—identified visually or confirmed statistically—are marked by alternating light blue and white bars. OM: organic matter, TIC: total inorganic carbon, χ_{LF}: low-frequency magnetic susceptibility, χ_{FS}: frequency-dependent magnetic susceptibility.

TIC, OM, grain size median diameter, and frequency-dependent MS ($\chi_{FS;}$ the change in MS measured at different field frequencies), calculated as:

$$\chi_{fs} = (\chi_{lf} - \chi_{hf})/(\ln f_{hf} - \ln f_{lf})$$

where f_{lf} and f_{hf} are the low and high frequencies used during the experiments, respectively.

The non-parametric Mann–Whitney statistical test, designed to compare two independent samples and assess whether their medians differ significantly, was employed to identify breaks in the time series. For this, a moving

window Mann-Whitney test was applied along the profile. For each time series, the first two samples on which the test was applied consisted of two non-overlapping, contiguous vertical windows of 19 samples. These windows were subsequently moved along the vertical profile at one data point at a time, defining in each step two new samples on which the test was applied. The depths at which the medians of the two samples were significantly different (p value <0.05) were defined as break-points in the time series.

2.7. Calculation of DMAR

The calculation of DMAR (mass distance^{-2} time^{-1}) was based on Cosentino et al. (2024), as:

$$\mathrm{DMAR} = \frac{h_{\mathrm{thick}} \times \mathrm{DBD} \times \mathrm{EC} \times f_x}{\Delta t}$$

where Δt is the time represented between two stratigraphic horizons (time), h_{thick} is the thickness between those two horizons (distance), DBD is the interval dry bulk density (mass distance^{-3}), EC (dimensionless) is the mass fraction corresponding to non-volcanic eolian mineral dust, and f_x (dimensionless) is the mass fraction of loess with particle diameters lower than a specific threshold (x).

We estimated DBD every 2.2 cm based on particle size and OM content using the Soil Water Characteristics software (Saxton & Rawls, 2006). For EC, we assumed that OM in loess is post-depositional in origin, and thus we subtracted the OM content to calculate EC (Cosentino et al., 2024). Furthermore, we subtracted 50% of the TIC to calculate EC, as it was assumed that 50% of the carbonate in loess is authigenic (Cosentino et al., 2024). Additionally, wet climatic conditions, such as during interglacials, were considered to deplete 10% of the primary carbonate content in soils (Meng et al., 2015, 2018; Z. Zhang et al., 2023). This post-depositional loss of carbonate was incorporated into EC calculations for the Holocene section of the Lozada loess profile. The calculation of the uncertainty in DMARs followed the approach outlined in Cosentino et al. (2024).

2.8. Analysis of Modeled Precipitation and Model-Data Comparison

Model simulations are a valuable tool for reconstructing past climatic conditions, especially in regions where proxy information is scarce or absent. To gain a more comprehensive understanding of the climatic controls on the properties and accumulation history of loess in SSA, we evaluated annual total precipitation output from coupled atmosphere-ocean simulations participating in the Paleoclimate Modeling Intercomparison Project (PMIP)-Phase 4 (PMIP4) for the present-day (1950–2014 Atacama Desert), mid-Holocene (MH: 6 ka) and LGM (defined in this context as 21 ka).

For the LGM versus present and LGM versus MH comparisons, simulations from a total of three models were considered, while 12 models were considered for the MH versus present comparison (Table S2 in Supporting Information S1). These models offer the highest horizontal resolution (~1° × 1° to ~2.5° × 2.5°) and are thus the most likely to best represent the spatial distribution of precipitation in regions with abrupt topography, such as the Andes. All simulation grids were interpolated to the coarsest grid for each comparison.

Additionally, a compilation of proxies representing past hydroclimate conditions in SSA (16–42°S, 45–75°W) was conducted. The proxies considered may directly describe paleo-precipitation at a specific site, but most often, they reflect more indirect aspects of the hydroclimate system. These proxies encompass a wide variety of records, including alluvial, moraine, lacustrine and salt deposits, ice cores, plant macrofossils, paleowetlands, paleodune sequences, soils, pollen, diatoms, as well as physico-chemical and isotopic proxies. In total, proxies from 44 sites were available that allowed a comparison of LGM and present conditions (Coppo et al., 2022; Maksic et al., 2022; Wainer et al., 2005). In turn, 51 indicators were compiled for the MH versus present comparison (Gorenstein et al., 2022; Orellana et al., 2023; Tchilinguirian & Morales, 2013). Finally, nine sites included proxy data for the LGM and MH comparison (Berman et al., 2018; Coppo et al., 2022). Table S3 presents the full list of proxies.

3. Results

3.1. Sediment Properties

The loess layers are light-colored and texturally heterogeneous, appear immediately below the BCk horizon, at approximately 1.4–1.5 mbs, and extend downward through the section. In this interval, discrete sub-horizontal

laminations (<2 cm thick) composed of fine sand, silt, and clay are particularly evident in the mid-section of the profile (e.g., around 3.2 mbs). Carbonate mobilization is evident through the development of calcitic nodules extending into the profile, particularly between 2.8 and 3.8 mbs. These features align with the descriptions provided by Kemp et al. (2006), who describe the upper section of the profile as a silty loam soil characterized by bioturbated and leached A and Bw horizons (above 1.4 mbs), and substantial secondary carbonate accumulation in the BCk and Ck horizons. There was no field evidence of either paraconformities or erosional unconformities in either the vertical or lateral exposures of the sequence.

The section exhibits a bimodal grain size distribution, with optical diameter modes of ∼14 and ∼50 μm (Figure 2a), and median values between ∼9 and 43 μm (Figure 2a). The OM content in Lozada generally ranges between ∼2%–5.5%, while TIC, estimated as carbonate content, varies between 1.7% and 5% (Figure 2a). χ_{LF} and χ_{FS} range between 1.6–3.1 and 0–0.29 × 10^{-6} m^3 kg^{-1}, respectively (Figure 2a).

3.2. New Regional Chronology

The De and dose rate data for the new quartz OSL and K-feldspar $pIRIR_{290}$ ages, along with previously reported quartz pIRSL-OSL ages from Torre et al. (2019) and K-feldspar $pIRIR_{290}$ ages from Coppo et al. (2022), as well as the newly modeled Bayesian ages, are available in the archived data set (Montecino Jara et al., 2026). The new ages (prior to Bayesian modeling; Figure 2a) follow a normal stratigraphic order, with only one age inversion. The overdispersion values remain below 35% (except for a single sample), indicating that sediment bleaching was complete and that no significant post-depositional mixing occurred (Arnold & Roberts, 2009).

To assess the bleaching efficiency of K-feldspar and evaluate potential overestimation in $pIRIR_{290}$ depositional ages, we analyzed both feldspar and quartz grains from a sample collected at 0.4 m depth (late Holocene). The $pIRIR_{290}$ age obtained was 10.58 ± 1.28 ka (37.1 ± 3.5 Gy; 12 aliquots), while the quartz OSL age at the same depth was 4.19 ± 0.43 ka (12.9 ± 0.7 Gy; 17 aliquots). Assuming that the age calculated using the Central Age Model for quartz is accurate and that both minerals are dating the same depositional event, the residual dose for the $pIRIR_{290}$ signal at the time of deposition can be estimated as approximately 24.2 ± 2.8 Gy, equivalent to an age of 6.4 ka. This finding suggests: (a) differential bleaching rates between quartz OSL and feldspar $pIRIR_{290}$ signals and (b) that, as numerous studies indicate (e.g., Buylaert et al., 2012; Perić et al., 2020; Yi et al., 2015), the bleaching of aeolian dust in natural settings likely occurs in repeated cycles over extended periods. With this in mind, we can assume that K-feldspar grains from Pampean loess has a relatively small residual dose prior at deposition, and their De estimated provides a reliable approximation of burial time, for the deeper intervals of the studied profile, more even if we consider that De recorded in this section are of the order of ∼100 Gy (Montecino Jara et al., 2026).

The Bayesian age estimates for the Lozada section, along with their 1σ confidence intervals, are presented in Figure 2b. The new Bayesian ages range from 1.7 ± 0.7 to 43.3 ± 1.9 ka, spanning approximately 42,000 years of dust deposition history in the Pampean plains. These ages encompass MIS3 (57–29 ka), the LGM (29–19 ka), the last deglaciation (19–14 ka), the Antarctic Cold Reversal (14–12 ka), and the Holocene (<11.7 ka). The new age data set presented here provides, for the first time, a continuous Pampean loess accumulation record throughout nearly the entire Holocene and extends the age range for MIS3 by approximately 5,000 years beyond the chronology reported by Coppo et al. (2022).

3.3. Proposed Stratigraphy

Based on an initial visual inspection and followed by a statistical approach, we divided the Lozada section into seven major units according to changes in median grain diameter, OM, TIC, and χ_{FS} (Figures 2a and 2c; Montecino Jara et al., 2026):

Unit 1 (4.8–3.8 mbs, 45.3–33.6 ka). Fine to medium yellowish-brown silt, with a median grain diameter between 8.5 and 17 μm, exhibiting low variability. No soil development is present, with low and stable OM and TIC. χLF remains stable, with values ranging from 2.1 to 2.3 × 10^{-6} m^3 kg^{-1}. χ_{FS} is relatively high (mean: 2.2 × 10^{-8} m^3 kg^{-1}), showing a decreasing trend toward the top of the unit (Figures 2a–2c).

Unit 2 (3.8–3.1 mbs, 33.6–25.0 ka). Yellowish silt, with abundant centimetric calcitic nodules. It is primarily composed of very coarse silt with a median grain diameter between 18 and 38 μm, which displays an abrupt rise at

the bottom of the unit. OM and TIC increase relative to Unit 1. χ_{FS} is relatively low (mean: 1.4×10^{-8} m^3 kg^{-1}), with a discrete peak at 3.6 mbs (Figures 2a–2c).

Unit 3 (3.1–2.7 mbs, 25.0–18.8 ka). Very coarse yellowish silt, with a median grain diameter between 31 and 43 μm, coarser than Unit 2, and increasing toward the top of the unit. With respect to Unit 2, OM remains stable while TIC first decreases and then increases again. χ_{FS} exhibits an increasing trend (Figure 2a–2c).

Unit 4 (2.7–1.9 mbs, 18.8–11.6 ka). Yellowish very coarse silt, with a median grain diameter between 33 and 44 μm. Grain size decreases toward the top of the unit. OM shows an increasing trend, while TIC decreases and subsequently increases. χ_{FS} generally decreases, but with high variability (Figures 2a–2c).

Unit 5 (1.9–1.3 mbs, 11.6–7.6 ka). Yellowish very coarse silt, with a median grain diameter between 21 and 42 μm, first increasing to a maximum around 9.8 ka, then decreasing toward the top of the unit. The presence of a Ck horizon indicates incipient soil development. OM remains stable, except for a peak near the base. TIC is more variable, reaching a maximum of 5% at 1.4 mbs, with a subsequent decline. Meanwhile, χ_{FS} follows a decreasing trend starting at the base, reaching a minimum around 9 ka, followed by a moderate upward trend, with a maximum at the top of the unit (Figures 2a–2c).

Unit 6 (1.3–0.8 mbs, 7.6–3.9 ka). Yellowish-brown very coarse silt, with a median grain diameter between 21 and 33 μm, showing a decreasing trend, with two major peaks near the base and top of the unit. Soil development is indicated by Bck and Ck horizons. OM follows an increasing trend, while TIC exhibits significant variability. χ_{FS} increases toward the top (Figures 2a–2c).

Unit 7 (0.8–0.4 mbs, 3.9–1.7 ka). Dark yellowish-brown very coarse silt, with median grain diameter between 21 and 34 μm, showing a decreasing trend toward the top of the unit with significant variability. Soil development is marked by a Bck horizon. OM and TIC follow similar trends, dropping sharply toward the top. Meanwhile, χ_{FS} shows an increasing trend toward the top of the unit (Figures 2a–2c).

3.4. Grain Size End-Members Analysis

The EMA indicates that ~98% of the data set variance is explained by three EMs (Figure 3a; Montecino Jara et al., 2026). Statistical diagnostics showed that improvements from one to three EMs are substantial, whereas additional components produce only marginal gains, supporting the selection of a 3-component model.

Their median values are 8.6 μm (EM1), 19 μm (EM2), and 54 μm (EM3; Figure 3a), which corresponds to fine, medium and coarse silt, respectively. A minor coarse tail is present in a few samples, but the EMA did not extract it as a separate component. We interpret this feature as locally derived lithogenic particles (>63 μm) that were not transported as part of the sustained aeolian suspension load, given that such coarse grains are rarely carried over long distances. Because this material represents only a very small fraction of the total volume and does not form a consistent modal peak, its limited representation in the model does not compromise the subsequent interpretations of the EMA.

These components exhibit significant variations over time (Figure 3b). EM3 is the most stable, with an average abundance of 46%. However, a sharp increase is observed between base and top of Unit 1 (45.3–33.6 ka). Conversely, EM3 increases between the base of Unit 3 and the top of Unit 4 (25–11.6 ka), followed by a decreasing trend toward the top of the section (11.6–1.7 ka). EM1, with an average abundance of 27%, is most dominant in the lower part of the sequence (Unit 1; 45.3–33.6 ka; Figure 3b). It then undergoes a sharp decline at the base of Unit 2 (33.6 ka), followed by a gradual increase. A decreasing trend is observed in Units 3 and 4 (25–11.6 ka). In the upper section (Units 5, 6, and 7; 11.6–1.7 ka), EM1 stabilizes, fluctuating between 11% and 26%. EM2 has a mean abundance of 27%. In the lower half of the record, its trend closely follows that of EM1 (Figure 3b). However, in the upper half, EM2 exhibits a distinct increasing pattern.

On the other hand, Cosentino et al. (2020) identified and characterized three end-members (EMs*; Figure 3a) in modern dust samples collected at Marcos Juárez (MJ) station, located in the core of the Pampean loess belt (Figure 1). This close analogy between modern and paleo-dust end-members allows us to infer the environmental significance of each EM in the loess record. The modern dust EMs closely resemble those observed in the Lozada loess profile, which have coarser median sizes, reflecting the influence of transport distance and associated particle size reduction. Previous studies have shown that both modern dust and paleo-dust originate from the same source regions (Cosentino et al., 2020; Gaiero et al., 2013; Gili et al., 2017; Torre et al., 2020, 2022), in this

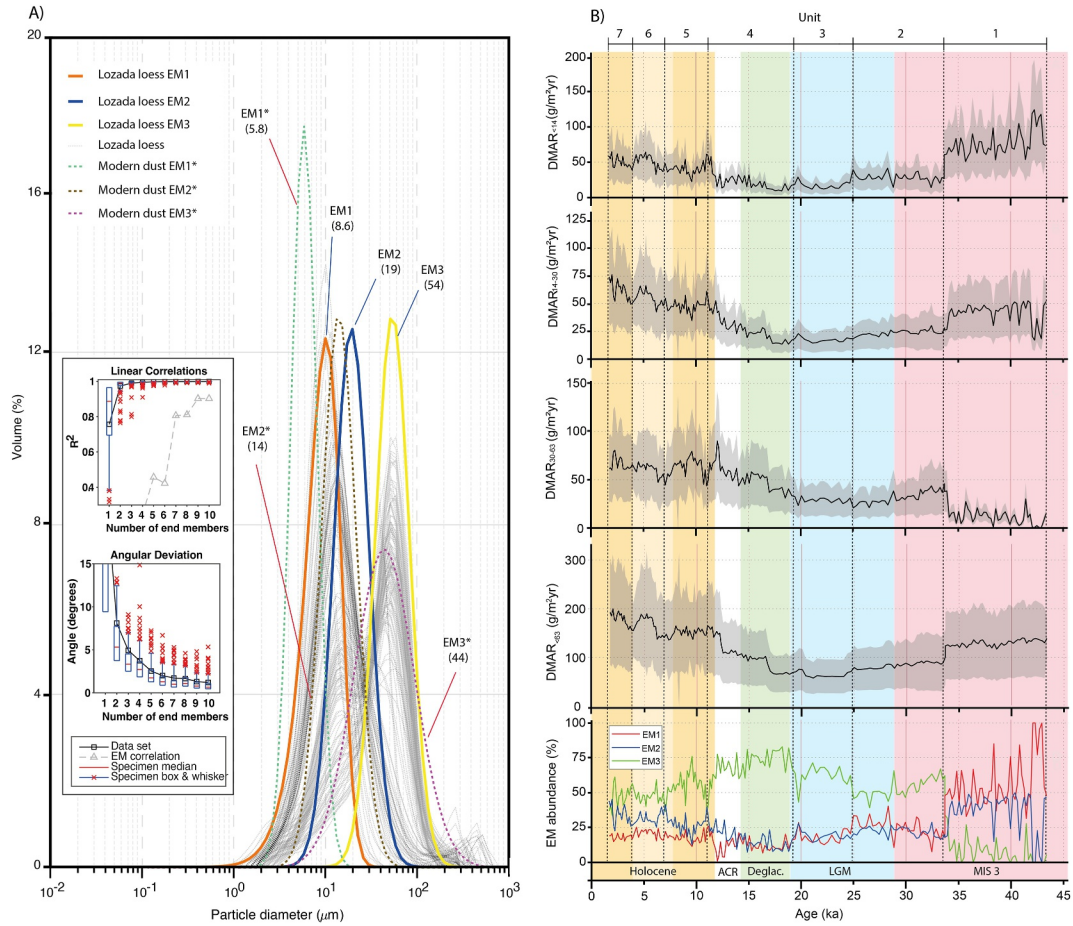

Figure 3. Grain-size distributions and end-member modeling results for the Lozada section. (a) Grain size distribution curves for the full data set (gray) and for the Lozada section. End-member (EM) curves for Lozada are shown in orange (EM1), blue (EM2), and yellow (EM3). Dashed green, brown, and violet lines represent EM1*, EM2*, and EM3*, based on modern dust samples from Marcos Juárez (Cosentino et al., 2021). An inset includes the statistical results of the grain size unmixing analysis for the Lozada samples. (b) Temporal variability of dust mass accumulation rates (DMARs) and grain-size end-members (EMs) for the Lozada section. From bottom to top, it presents changes in the proportions of identified end-members, followed by DMARs for different grain size fractions: <63, 30–63, 14–30, and <14 μm.

context, the finer grain sizes at MJ likely reflect greater atmospheric transport and preferential removal of coarser particles before reaching the sampling site (Pye & Tsoar, 1987; Vandenberghe, 2013).

3.5. Loess Dust Mass Accumulation Rates

DMARs and their 1σ confidence intervals, based on the age-depth model, are presented in Figure 3b and in the associated data set (Montecino Jara et al., 2026). DMAR was calculated for the grain size fraction of loess with particle diameters lower than 63 μm ($DMAR_{<63}$). This threshold, consistent with the conventional boundary between silt and sand, allows us to separate dust particles that are susceptible to prolonged atmospheric transport (≤63 μm) from sand-sized particles (>63 μm), which are rarely transported over long distances and could include lithogenic components that are not strictly eolian in origin (e.g., Adebiyi et al., 2023; Kok et al., 2012). Additionally, DMARs were estimated for the granulometric fractions corresponding to the three identified EMs (Figure 3a), with cut-off sizes at 14 and 30 μm ($DMAR_{<14}$, $DMAR_{14–30}$, $DMAR_{30–63}$).

Studies conducted on modern dust in the region (Cosentino et al., 2020; Torre et al., 2020) suggest that these fractions reflect: (a) long-distance (≥1,000 km) (14–30 μm and <14 μm; Pye & Zhou, 1989; X. Y. Zhang et al., 1997) and short-distance (several tens to hundreds of kilometers) (30–63 μm; Pye & Zhou, 1989;

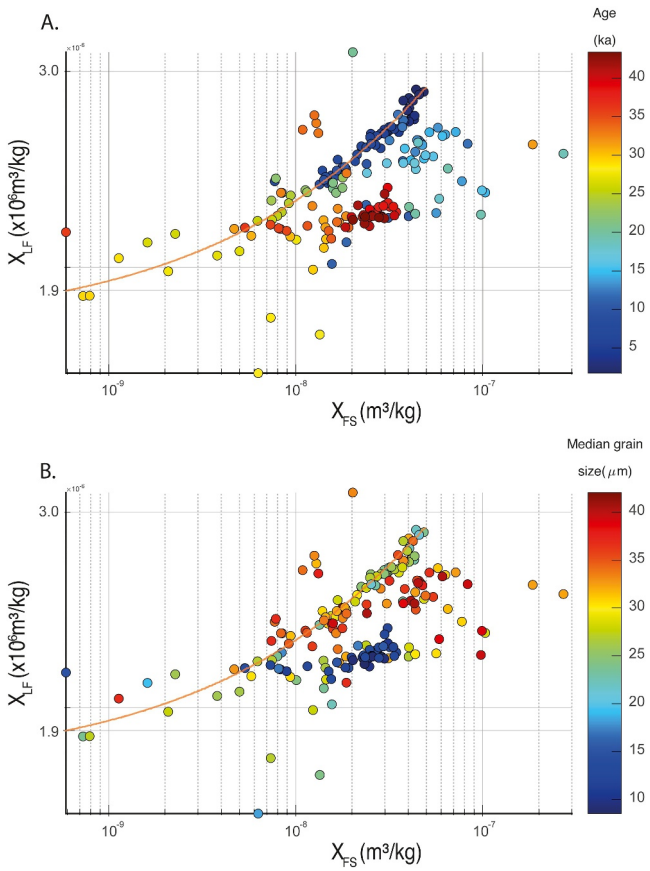

Figure 4. Relationship between χ_{FS} and χ_{LF} for the complete Lozada data set, and their association, according to the color scale, with: (a) the age of the analyzed samples, and (b) the median grain size. The linear trend describing the magnetic enhancement of loess during pedogenesis, commonly referred to as the "true loess line," is shown as an orange curve.

Vandenberghe, 2013) transport, and (b) dry-dominated (30–63 μm; Cosentino et al., 2020; Torre et al., 2020), wet-dominated (<14 μm), and dry-wet mixed (14–30 μm) deposition (Cosentino et al., 2020; Torre et al., 2020).

The highest $DMAR_{<63}$ are observed during the Holocene, with values ranging from 136 (±76) to 199 (±12) g m^{-2} yr^{-1}. In contrast, the lowest $DMAR_{<63}$ occur during the LGM (from 57 ± 33 to 85 ± 49 g m^{-2} yr^{-1}). The increase in $DMAR_{<63}$ begins during the onset of the last deglaciation. This trend continues until ~12 ka, when $DMAR_{<63}$ stabilizes. Instead, $DMAR_{14–30}$ continues to rise until the top of the profile. During MIS3 (~45–34 ka), the $DMAR_{<14}$ and $DMAR_{14–30}$ reach relatively high values. In contrast, $DMAR_{30-63}$ reaches its minimum values during this interval. Finally, between the late MIS3 and early LGM (~34–25 ka), all DMARs exhibit a declining trend.

3.6. Magnetic Enhancement Trends

Figure 4 illustrates the relationship between χ_{FS} and χ_{LF} in the Lozada section, with colors representing sample ages based on the age-depth model (Figure 4a) and median grain diameter (Figure 4b). The Pearson correlation coefficient is high (r = 0.9) for Holocene samples (~1.7–10 ka). However, some samples deviate from this trend, exhibiting higher χ_{LF} values. These samples generally have median grain diameters >32 μm, exceeding the overall median average (31 μm), with no clear relationship to age. Most correspond to deposits from the LGM and early MIS3.

Additionally, some samples deviate toward higher χ_{FS}. Like the previously mentioned samples, they have median grain diameters above the average and cluster temporally between ~12 and 19 ka. Finally, another subset of samples, primarily from the early Holocene and MIS3, exhibits lower-than-average median grain diameters (<31 μm) and low χ_{LF}.

3.7. Paleo-Precipitation Based on PMIP4 Simulations

Several studies have analyzed regional climatic characteristics in SSA during the LGM and the MH using various paleoclimatic simulations produced by PMIP Phase III (PMIP3; Berman et al., 2016, 2017, 2018; Coppo et al., 2022; Prado et al., 2013). Here, we evaluate PMIP4 simulations to explore how differences in precipitation between the LGM and the MH influenced mineral dust aerosol emissions at source regions and subsequent dust accumulation in the Pampean plains. Changes in precipitation patterns can strongly influence dust accumulation rates, particularly through wet deposition processes that primarily control the accumulation of fine particles (Miller et al., 2006; Woodward, 2001; Zender et al., 2003).

According to the PMIP4 model simulations, the western slope of the central Andes experienced wetter conditions during the LGM compared to the present (Figure 5a). Wetter conditions also extended to the Altiplano and some sectors of the northern and southern Puna. These results broadly align with most compiled proxy records. In contrast, extra-Andean eastern Patagonia, the southern Andes (37–52°S), and the Pampean region were generally drier than today, a pattern also supported by available paleoclimatic records. In SCWA, the models suggest wetter conditions, with a transition to drier conditions toward the east.

For the MH, simulations indicate that areas south of 30°S on the western slope of the Andes remained wetter than present, while north of 30°S the models disagree (white pixels) and the proxies generally show drier conditions (Figure 5c). On the eastern slope of the Andes, proxies indicate increased humidity in the PAP and the southern SCWA, whereas the models again suggest drier-than-present conditions. These mismatches may be attributed to the models' limited spatial resolution (Coppo et al., 2022). While we restricted our analysis to simulations with the greatest resolutions, these may still be low enough to hinder the accurate representation of first-order precipitation

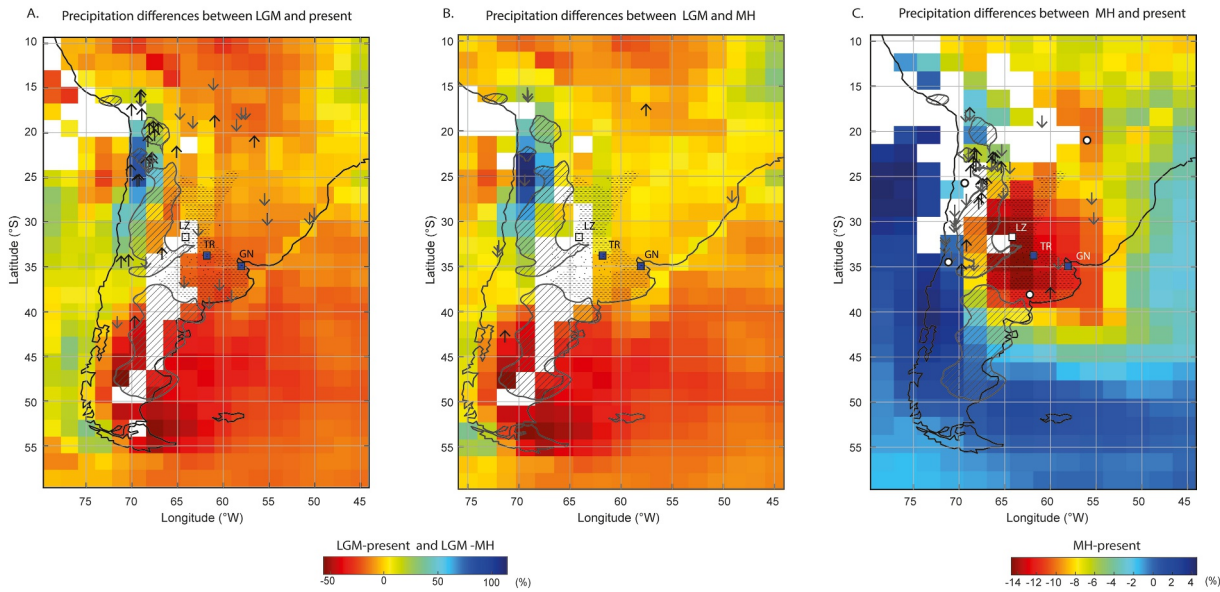

Figure 5. Mean annual precipitation across different periods: (a) Last Glacial Maximum (LGM) versus present, (b) LGM versus Mid-Holocene (MH), and (c) MH versus present. Percentage changes in precipitation were calculated relative to the reference period for each case. Shifts toward blue colors indicate wetter conditions relative to the reference period, while shifts toward red colors indicate drier conditions. Panels (a) and (b) share the same color scale, while panel C uses a different scale to enhance the visualization of MH–PRE differences, which would be difficult to discern if the same scale were maintained. White pixels indicate low model agreement (1σ/mean ≥ 0.5). Arrows represent proxy-based paleo-precipitation data: upward for wetter, downward for drier conditions, and white dots for no significant change. The Lozada section is marked with a white square; blue squares mark Tortugas and Gorina.

gradients along the Andes. In the Pampean region, the models simulate drier conditions during the MH than at present, but proxy data for this area remain inconclusive.

When comparing the LGM and MH, both the compiled proxies and model results generally agree (Figure 5b). The models indicate wetter conditions during the LGM than during the MH along the western slope of the Andes and in the region between 15° and 35°S west of 60°W. Further east, in a portion of the Pampean region, this relationship reverses. Here, the models suggest wetter conditions during the MH, a trend that extends to the Atlantic coast. In Patagonia, the models indicate drier conditions during the LGM compared to the MH.

4. Discussion

4.1. Processes Influencing Magnetic Enhancement

Two widely accepted conceptual frameworks explain increases in MS parameters in loess-paleosol sequences: the pedogenic and the wind vigor models (Evans, 2001; Evans & Heller, 1994; Forster et al., 1994). The pedogenic model attributes increases in both χ_{LF} and χ_{FS} to the in situ formation of magnetic minerals during soil development (Dearing et al., 1996; Forster et al., 1994; Heller et al., 1993; Maher, 2011, 2016; Maher & Taylor, 1988), particularly in interglacial soils, where warmer temperatures and higher precipitation favor the formation of ultrafine magnetic grains. The linear trend representing loess magnetic enhancement through pedogenesis is often referred to as the "true loess line" (Forster et al., 1994; Maher, 2011; Panaiotu et al., 2001; Zeeden et al., 2016). In contrast, the wind vigor model explains higher χ_{LF} values in loess (rather than in paleosols) as the result of selective enrichment of coarser magnetic minerals in units dominated by larger particles (Evans, 2001).

However, magnetic minerals are susceptible to alteration in varying environmental settings (Hu et al., 2013; Orgeira et al., 2011), making reconstructions based solely on loess–paleosol MS records more complex than initially assumed (Hu et al., 2015; Orgeira & Compagnucci, 2006). Recognizing this, Liu and Mao (2021) proposed a model relating MS to effective precipitation (precipitation minus evaporation), categorizing three scenarios to interpret MS patterns across climatic gradients.

In hyper-arid areas close to dust sources, physical weathering dominates and pedogenesis is limited, resulting in MS values that primarily reflect the concentration of coarse-grained magnetic minerals, with a negative

relationship between MS and pedogenesis (Song et al., 2010; Zan et al., 2010, 2012). In transitional arid settings, farther from sources, a weak correlation between MS and pedogenesis is observed (Liu et al., 2017). With increasing effective precipitation, pedogenesis intensifies, evidenced by processes such as carbonate leaching and the development of features like filaments, nodules, and carbonate-rich horizons (Zamanian et al., 2016). However, beyond an effective precipitation upper threshold, seasonal water saturation can promote the transformation of iron oxides into hydroxides (e.g., goethite), reducing MS (Han et al., 1996; Liu & Mao, 2021; Maher & Thompson, 1995).

Given the sensitivity of MS to pedogenic processes and soil moisture, its interpretation must be contextualized within a broader framework of complementary pedogenic indicators. These include soil color (as a proxy for redox conditions), paleosol structures (reflecting the intensity of soil development), and sediment physical parameters such as grain size distribution (Liu & Mao, 2021). In this context, our results from the Lozada section suggest that the MS signal reflects the combined influence of multiple mechanisms of magnetic enhancement at the western margin of the Pampas.

In the Lozada section, the Pearson correlation coefficient between χ_{FS} and χ_{LF} is high ($r = 0.9$) for the set of Holocene samples (Units 5–7). This is consistent with pedogenic enhancement under oxidizing conditions, as evidenced by features such as soil color, the presence of pedogenic carbonates, spongy microstructure, and bioturbation in the upper stratigraphy (Bradák et al., 2021; Liu & Mao, 2021).

However, several samples, primarily from LGM (Unit 3) and late MIS3 (Unit 2), display two distinct patterns. One subset aligns with the lower part of the pedogenic enhancement trend, suggesting incipient pedogenic enhancement. Another subset departs from this trend, exhibiting higher χ_{LF} values. These samples tend to have median grain diameters exceeding the average median and show no clear age dependence. This dispersion can be explained by the wind vigor model, as an increase in median grain diameter and in the proportion of EM3 suggest generally stronger wind conditions (Bradák et al., 2021; Liu & Mao, 2021).

Additionally, some samples of last deglaciation and ACR age (Unit 4) deviate toward higher χ_{FS}. They also possess median grain diameters and proportion of EM3 above the sequence averages, suggesting a period likewise associated with enhanced wind activity (Figure 4). A possible explanation, as suggested by Bradák et al. (2021), is the formation of nanoscale magnetic particles by fragmentation during aeolian transport (e.g., through grain collisions). This nano-fragmentation process increases χ_{FS} without substantially altering χ_{LF}, since the total concentration of magnetic minerals remains unchanged, a scenario consistent with intensified physical weathering during transport under stronger wind conditions.

Finally, a subset of samples, primarily from MIS3 (Unit 1), display lower-than-average median grain diameters (<31 μm) and low χ_{LF} values. This trend is attributed to a reduction in the magnetic signal through dissolution (Bradák et al., 2021), likely associated with hydromorphic processes such as prolonged water saturation or intense chemical weathering (Zeeden et al., 2018a, 2018b). According to Liu and Mao (2021), this phenomenon typically occurs under conditions of abundant rainfall, fluctuating water tables, or seasonal waterlogging.

4.2. Controlling Factors for Dust Emissions and Loess Accumulation

To investigate paleoclimatic patterns and shifts in sediment availability influencing loess accumulation in the Pampean region, a comparative chart was constructed (Figure 6). This integrates diverse paleoclimate proxies from SSA's main dust source areas (Figures 6a–6f) with DMARs from the Lozada section (this study; Figures 6g–6j) and <63-μm DMARs from Tortugas and Gorina sections (Figures 6k and 6l; Figure 1; Coppo et al., 2022). To avoid confusion, it should be noted that the proxy compilations in Figures 5 and 6 differ in scope. Figure 5 addresses qualitative moisture variability during the LGM and MH, whereas Figure 6 incorporate records reflecting not only paleohydrological conditions but also sediment supply and geomorphological processes. Based on this regional compilation of paleoclimate proxy information, we define the following regional paleoclimate phases:

Phase 1: Abrupt decrease in wet accumulation (45.3–33.6 ka). Evidence from tufa deposits and gamma radiation records at Salar de Uyuni indicates wetter conditions at PAP between 45 and 39 ka (Baker et al., 2001; Placzek et al., 2006). Earlier, two major lacustrine phases between 120–98 and 95–80 ka also reflect wetter periods (Placzek et al., 2006). In the Puna, Pozuelos Lake records show a positive precipitation-evaporation balance until ca. 36 ka (McGlue et al., 2013). Glacial advances at 24°S and 26°S around 40 ka support this regional humidity

10.1029/2025PA005304

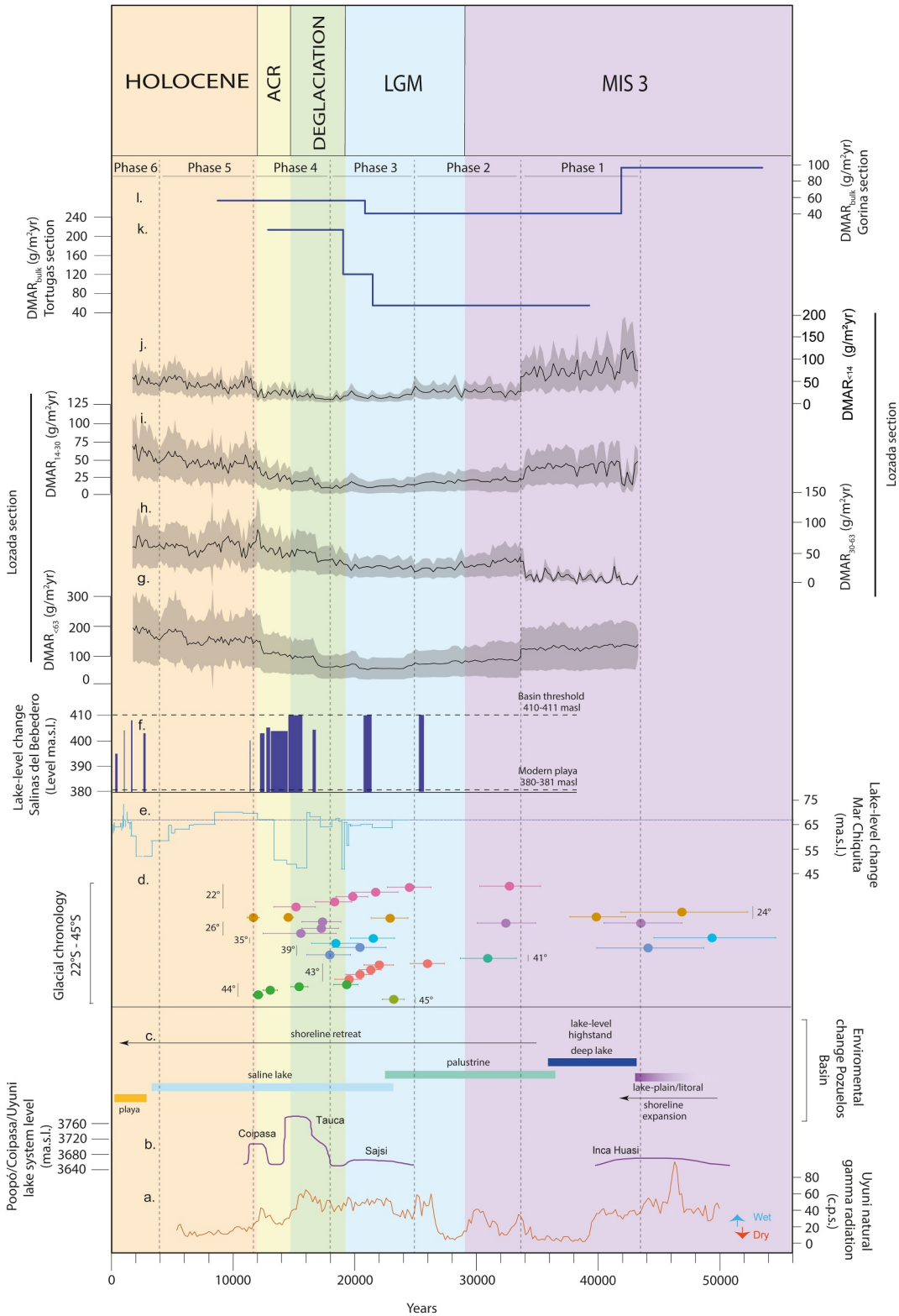

Figure 6.

(Martini et al., 2017; J. Zech et al., 2017). Despite these wetter intervals, sediment from previous lake high-stands (115–100 ka) and long-term landscape stability (Toledo Geosol; Placzek et al., 2006) left the Altiplano with ample dust supply between 95 and 45 ka. In Patagonia, evidence of older glacial advances (Hein et al., 2017; Leger et al., 2023; Mendelová et al., 2020; Peltier et al., 2023; J. Zech et al., 2017) suggests active dust sources on relict outwash plains. On the other hand, based on the geomorphology, facies analysis and fossil content, Kruck et al. (2011) recognize a humid phase in the Chaco-Pampean plains between 28 and 41 ka. This is also concordant with the MS data of the analyzed samples of Unit 1, that suggest water saturation or intense chemical weathering typically linked to conditions of abundant rainfall, fluctuating water tables, or seasonal waterlogging according to Liu and Mao (2021).

At Lozada, $DMAR_{<63}$, $DMAR_{<14}$ and $DMAR_{14\text{-}30}$ all decreased between 43 and 33 ka. $DMAR_{30\text{-}63}$ reached its lowest value, suggesting that during this interval, wet deposition dominated dust input. This aligns with the wetter conditions in the Pampean plains suggested by Kruck et al. (2011), and increased dust supply from the PAP, consistent with DMAR values and isotopic signatures reported by Coppo et al. (2022) for the Gorina section.

Phase 2: Slight decrease in wet accumulation (33.6–25.0 ka). Paleoclimate records indicate increasing aridity in the southern Puna and Altiplano between ∼36 and 25 ka (Baker et al., 2001; McGlue et al., 2013; Placzek et al., 2013). However, limited data from northern Patagonia and SCWA during this interval hinders interpretation in other potential dust source regions. In contrast, the Chaco-Pampean plains experienced wetter conditions initially, turning arid by ∼28 ka with only weak humid episodes (Kruck et al., 2011).

The estimated DMARs from Lozada show a decreasing trend for $DMAR_{<63}$. A similar pattern is observed for the finer fractions. In contrast, the $DMAR_{30–63}$ displays a slight increase. These patterns suggest a reduction in dust contribution from distant sources, and a relative increase in dust supplied by proximal sources, reflected in the growing proportion of coarse particles. The increase in coarse particles is consistent with the MS signal for late MIS3 (Unit 2) that suggests stronger wind conditions, likely associated with an intensification, strengthening, or a northward latitudinal shift of the SWW.

These patterns agree with Coppo et al. (2022), who reported low DMARs in the Pampean plains during late MIS3 and the early LGM, along with reduced dust supply from the PAP, a trend also supported by isotopic evidence from Torre et al. (2022). The decline in fine particle accumulation reflects decreased sediment availability in distant sources like the PAP due to limited sediment recharge.

Phase 3: Enhanced aridity in the Pampean plains, wetter conditions in distal dust sources and minimum DMARs (25.0–18.8 ka). Proxy records suggest wetter and cooler conditions on the Altiplano and Northern Puna (NP) between ∼25 and 19 ka, as indicated by a modest expansion of the Poópo/Coipasa/Uyuni Lake system (Baker et al., 2001; Placzek et al., 2013), and by glacial geochronology from the eastern Andes (22°–24°S; Martini et al., 2017; R. Zech et al., 2008; J. Zech et al., 2017). These humid conditions likely reduced dust availability. However, some areas within the NP may have experienced increased aridity during this period. For example, the Late Quaternary stratigraphy and sedimentology of Pozuelos basin shows evidence of drier conditions between ∼26 and 23 ka (McGlue et al., 2013), which could have favored sediment deflation and positioned this region as a potential dust source. Further south (28°–34°S), flood deposits near Salinas del Bebedero indicate increased humidity in SCWA (Quade et al., 2022), where glacial and fluvial activity during wetter periods likely promoted sediment production. South of 34°S, glacier advances in southern SCWA and northern Patagonia (J. Zech et al., 2017) would have generated abundant fine sediments, which became available for deflation once exposed.

Both the accumulation rates calculated for Lozada (this study) and those estimated by Coppo et al. (2022) for the Tortugas and Gorina sections reach their minimum values during the LGM (∼24–20 ka). At Lozada, DMARs for fine distal fractions (<14 μm and 14–30 μm) drop significantly. The decline in DMARs linked to distal sources aligns with wetter conditions in potential source areas and increased aridity in the Pampean region, as shown by

Figure 6. Estimated dust mass accumulation rates (DMARs) from the Lozada section with regional paleohumidity records. It includes <63-μm DMARs for the l. Gorina and (k) Tortugas sections (Coppo et al., 2022), and Lozada DMARs for different grain size fractions: (g) <63 μm, (h) 30–63 μm, (i) 14–30 μm, and (j) <14 μm. Shaded areas indicate 1-sigma uncertainties. The DMAR trends are compared to (f) water level changes at Salinas del Bebedero (Quade et al., 2022), (e) Mar Chiquita Lake fluctuations (Cuña-Rodríguez et al., 2020), (d) Compiled glacial chronologies from the Andes (Leger et al., 2021; Martini et al., 2017; Peltier et al., 2023; Soteres et al., 2022; J. Zech et al., 2017), (c) environmental changes at Laguna Pozuelos (McGlue et al., 2013), (b) Paleolake reconstructions from the Altiplano (Placzek et al., 2013), and (a) Gamma radiation records from Uyuni (Baker et al., 2001).

the paleoprecipitation index in Figure 5a. This agrees with the reconstructed scenario by Cuña-Rodríguez et al. (2020), based on the Mar Chiquita Lake level. However, stable DMARs for coarser, locally sourced dust (SCWA and northern Patagonia) suggest these proximal sources remained active, continuously supplying material susceptible to dry deposition. This pattern is also consistent with the MS results, which show an increase in magnetic signal associated with a wind-vigor model. The enhanced MS signal and the dominance of coarser fractions together point to a strengthened and sustained influence of the SWW.

Phase 4: Dust deposition in the Pampean region under wetter but windier conditions (18.8–11.6 ka). Between ca. 18–12 ka, paleoclimatic indicators suggest wetter conditions in both the Altiplano and SCWA (Baker et al., 2001; Placzek et al., 2013; Quade et al., 2022). During this period, the Altiplano was home to paleolake Tauca. This lake began to rise between 18 and 17 ka, reaching its hydrologic maximum between 16.4 and 14.1 ka, then declined after 14 ka (Placzek et al., 2006). A brief resurgence, known as the Coipasa Lake phase, occurred between 13 and 11 ka (Placzek et al., 2006). These lake highstands broadly overlap with the hydrologic maximum and flooding of Laguna Bebedero (15.67–14.43 and 13–11 ka) (Quade et al., 2022). The wet period coincided with glacier advances in the arid Andes, driven by increased precipitation from a southward shift of the South American Summer Monsoon (Martini et al., 2017; J. Zech et al., 2017). These wet and dry phases were also recorded in the Pampean plains as changes in physical and isotopic indicators, as well as variations in the reconstructed lake level of the Mar Chiquita Lake (Cuña-Rodríguez et al., 2020). Meanwhile, in southern Puna, sedimentary facies suggest arid conditions during this period (McGlue et al., 2013).

$DMAR_{<63}$ from the Lozada increased significantly, with slight rises in fine DMARs (<14 μm and 14–30 μm). A larger increase is observed in $DMAR_{30–63}$. The slight increase in DMARs linked to distal sources aligns with wetter conditions in these regions, while stable EM3 values and continued sediment supply from nearby sources (SCWA, northern Patagonia) indicate these areas remained active. MS signal of the analyzed samples suggests intensified physical weathering during transport under stronger wind conditions, possibly as a result of a sustained influence of the SWW. On the other hand, according to Coppo et al. (2022), an increase in DMAR values at the Gorina and Tortugas loess section is observed over the same period.

Phase 5: Regional aridification, enhanced sediment availability and increase in wet accumulation (11.6–3.9 ka). Between 12 and 4 ka, sustained regional aridification is documented in the Altiplano (Baker et al., 2001; Placzek et al., 2013), southern Puna (McGlue et al., 2013), and SCWA (Quade et al., 2022), creating ideal conditions for sediment deflation. Prior high lake stands left abundant exposed sediments available for aeolian transport. In the Pampean region, a highstand phase in Mar Chiquita Lake during the Early Holocene was followed by declining lake levels and reduced precipitation, reaching a MH lowstand (Cuña-Rodríguez et al., 2020). This drying trend is consistent with widespread Early Holocene aridity in SSA at both sides of the Andes (Abarzúa & Moreno, 2008; Iglesias et al., 2011; Llano et al., 2020; Porras et al., 2012; Whitlock et al., 2006).

$DMAR_{<63}$ from the Lozada section increased significantly between 12 and 8 ka. $DMAR_{<14}$ and $DMAR_{14–30}$ showed similar upward trends, while $DMAR_{30–63}$ rose only slightly. The sharp rise in fine dust from distal sources reflects increased aridity and sediment availability in PAP, alongside relatively wetter conditions in the Pampean plains, which aligns with the paleoprecipitation index in Figures 5b and 5c. Despite the decrease in precipitation rates over the Pampean plains, we suggest that moisture conditions were still sufficient to favor wet deposition, which were greater than those prevailing during the LGM (Figure 5b). Meanwhile, the moderate increase in $DMAR_{30-63}$ suggests that dust from proximal sources (i.e., SCWA, northern Patagonia) was modulated by changes in wind speed and a weakening of the SWW during this period.

Phase 6: Increased wet accumulation driven by sediment availability and rising precipitation in the Pampean plains (<3.9 ka). After 4 ka, continued aridification in the Altiplano and southern Puna (Baker et al., 2001; Martini et al., 2017; McGlue et al., 2013; Placzek et al., 2013) enhanced sediment availability. Similarly, Quade et al. (2022) report extreme aridity at Salinas del Bebedero, with no flood deposits, suggesting no significant precipitation or ice accumulation in SCWA. Concurrently, increased precipitation in the Pampean plains (Cuña-Rodríguez et al., 2020) favored loess accumulation. This is consistent with soil developed in the upper stratigraphic unit, the presence of pedogenic carbonates, spongy microstructure, and with the pedogenic enhancement of the MS signal recorded in the Holocene samples (Units 5–7).

Expanded provenance study of this aeolian section is necessary to support interpretations about sediment availability and environmental conditions in the dust source areas through the time-lapse under study. This would also help explain the wind patterns responsible for transporting dust toward the Pampean region.

5. Conclusions

This study reconstructs dust emission, transport, and accumulation dynamics in SSA over the past 43 ka, using multiproxy data from the Lozada loess section. Dust fluxes were driven by interactions between hydroclimate variability, sediment availability, and large-scale atmospheric circulation. Moisture and temperature fluctuations controlled sediment supply in source areas, while shifts in the STJ, SWW, and Zonda winds regulated dust transport. Precipitation changes affected both sediment deflation and deposition via wet scavenging in the Pampean plains. The temporal patterns of dust accumulation documented in the Lozada section indicate: (a) high DMAR during MIS3 due to abundant sediment supply in dust sources and wetter conditions in the Pampas that enhanced wet dust deposition, (b) a marked decline during the LGM, linked to wetter source areas limiting deflation and enhanced aridity in the Pampean plains reducing wet dust deposition, and (c) a recovery in DMAR during the deglaciation and Early Holocene, associated with alternating wet/dry phases that recharged sediment supply at the sources, subsequent increased aridity in source areas, and high hydroclimatic variability in the Pampean plains.

Our DMAR data reveal millennial-scale fluctuations in dust accumulation, which cannot be explained solely by short-term meteorological variability. These patterns support the idea that large-scale reorganizations of the SWW and the STJ, orbitally modulated changes in the frequency of cold surges, and shifts in the position of the polar front have played a dominant role in controlling dust emissions over longer timescales.

Future research should focus on expanding the provenance analyses of this aeolian section, including the depths sampled in this study, to refine interpretations of sediment availability and past environmental conditions. This would improve reconstructions of ancient wind patterns and dust transport pathways, contributing to a better understanding of the links between atmospheric circulation, climate variability, and dust dynamics in SSA during the late Quaternary. Additionally, as dust from SSA is thought to represent an important source to the South Atlantic Ocean, identifying its provenance and quantifying its fluxes is essential for assessing its potential biogeochemical impacts on ocean productivity, nutrient cycling, and its possible role in modulating past and present climate systems.

Conflict of Interest

The authors declare no conflicts of interest relevant to this study.

Data Availability Statement

The data supporting this study are publicly available in Zenodo (Montecino Jara et al., 2026). The dataset includes luminescence dating results (equivalent doses, dose rates, and ages) for the Pampean loess sections, and stratigraphic, chronological, magnetic, and dust mass accumulation rate data for the Lozada section. All data are provided as .xlsx files.

Acknowledgments
This work was financed by project PICT-2021-I-A-00275 (Agencia I+D+i, Argentina), CONSOLIDAR-SECyT-UNC (2023–2027) and Fundación Williams to DMG and by project FONDECYT-POSTDOC2020-3200085 (ANID, Chile) to NJC. The discussions that resulted in this paper also benefited from meeting travel grants from project CLIMAT-AmSud 22-CLIMAT-01. It was also supported by the International Association of Sedimentologists Doctoral Grant and by the Quaternary Research Association New Research Workers Grant to DMJ. AOS is funded by the Conselho Nacional de Desenvolvimento Científico e Tecnológico (CNPq Grant 307179/2021-4).

References

Abarzúa, A. M., & Moreno, P. I. (2008). Changing fire regimes in the temperate rainforest region of southern Chile over the last 16,000 yr. *Quaternary Research*, *69*, 62–71.

Adebiyi, A., Kok, J. F., Murray, B. J., Ryder, C. L., Stuut, J.-B. W., Kahn, R. A., et al. (2023). A review of coarse mineral dust in the Earth system. *Aeolian Res*, *60*, 100849. https://doi.org/10.1016/j.aeolia.2022.100849

Arnold, L. J., & Roberts, R. G. (2009). Stochastic modelling of multi-grain equivalent dose (De) distributions: Implications for OSL dating of sediment mixtures. *Quaternary Geochronology*, *4*(3), 204–230. https://doi.org/10.1016/j.quageo.2008.12.001

Baker, P. A., Rigsby, C. A., Seltzer, G. O., Fritzs, S. C., Lowenstein, R. K., Bacher, N. P., & Veliz, C. (2001). Tropical climate changes at millennial and orbital timescales on the Bolivian Altiplano. *Nature*, *409*(6821), 698–701. https://doi.org/10.1038/35055524

Berman, A. L., Silvestri, G. E., Rojas, M., & Tonello, M. S. (2017). Accelerated greenhouse gases versus slow insolation forcing induced climate changes in southern South America since the Mid-Holocene. *Climate Dynamics*, *48*(1–2), 387–404. https://doi.org/10.1007/s00382-016-3081-z

Berman, A. L., Silvestri, G. E., & Tonello, M. S. (2016). Differences between Last Glacial Maximum and present-day temperature and precipitation in southern South America. *Quaternary Science Reviews*, *150*, 221–233. https://doi.org/10.1016/j.quascirev.2016.08.025

Berman, L., Silvestri, G., & Tonello, M. S. (2018). On differences between Last Glacial Maximum and Mid-Holocene climates in southern South America simulated by PMIP3 models. *Quaternary Science Reviews*, *185*, 113–121. https://doi.org/10.1016/j.quascirev.2018.02.003

Blaauw, M., & Christen, J. A. (2011). Flexible paleoclimate age-depth models using an autoregressive gamma process. *Bayesian Analysis*, *6*(3), 457–474. https://doi.org/10.1214/11-BA618

Blisniuk, P. M., Stern, L. A., Chamberlain, C. P., Idleman, B., & Zeitler, P. K. (2005). Climatic and ecologic changes during Miocene surface uplift in the Southern Patagonian Andes. *Earth and Planetary Science Letters*, *230*(1–2), 125–142. https://doi.org/10.1016/j.epsl.2004.11.015

Bradák, B., Seto, Y., Stevens, T., Újvári, G., Fehér, K., & Költringer, C. (2021). Magnetic susceptibility in the European Loess Belt: New and existing models of magnetic enhancement in loess. *Palaeogeography, Palaeoclimatology, Palaeoecology*, *569*, 110329.

Bruniard, E. (1982). La diagonal árida Argentina: Un límite climático real. *Revista Geografica*, *95*, 5–20.

Bullard, J. E., Harrison, S. P., Baddock, M. C., Drake, N., Gill, T. E., McTainsh, G., & Sun, Y. (2011). Preferential dust sources: A geomorphological classification designed for use in global dust-cycle models. *Journal of Geophysical Research*, *116*(F4), F04034. https://doi.org/10.1029/2011jf002061

Buylaert, J. P., Jain, M., Murray, A. S., Thomsen, K. J., Thiel, C., & Sohbati, R. (2012). A robust feldspar luminescence dating method for middle and Late Pleistocene sediments. *Boreas*, *41*(3), 435e451. https://doi.org/10.1111/j.1502-3885.2012.00248.x

Clark, P. U., Dyke, A. S., Shakun, J. D., Carlson, A. E., Clark, J., Wohlfarth, B., et al. (2009). The Last Glacial Maximum. *Science*, *325*(5941), 710–714. https://doi.org/10.1126/science.1172873

Coppo, R., Cosentino, N., Torre, G., del Rio, I., Sawakuchi, A., Berman, A., et al. (2022). Coeval minimum South American and maximum Antarctic Last Glacial Maximum dust deposition: A causal link? *Quaternary Science Reviews*, *295*, 107768. https://doi.org/10.1016/j.quascirev.2022.107768

Cosentino, N. J., Gaiero, D. M., & Lambert, F. (2021). Present-day Patagonian dust emissions: Combining surface visibility, mass flux, and reanalysis data. *Journal of Geophysical Research: Atmospheres*, *126*(16), e2020JD034459. https://doi.org/10.1029/2020JD034459

Cosentino, N. J., Gaiero, D. M., Torre, G., Pasquini, A. I., Coppo, R., Arce, J. M., & Vélez, G. (2020). Atmospheric dust dynamics in southern South America: A 14-year modern dust record in the loessic Pampean region. *The Holocene*, *30*(4), 575–588. https://doi.org/10.1177/0959683619875198

Cosentino, N. J., Torre, G., Lambert, F., Albani, S., De Vleeschouwer, F., & Bory, A. J.-M. (2024). Paleo±Dust: Quantifying uncertainty in paleodust deposition across archive types. *Earth System Science Data*, *16*(2), 941–959. https://doi.org/10.5194/essd-16-941-2024

Csavina, J., Field, J., Félix, O., Corral-Avitia, A. Y., Sáez, A. E., & Betterton, E. A. (2014). Effect of wind speed and relative humidity on atmospheric dust concentrations in semi-arid climates. *Science of the Total Environment*, *487*, 82–90. https://doi.org/10.1016/j.scitotenv.2014.03.138

Cuña-Rodríguez, C., Piovano, E. L., García-Rodríguez, F., Sylvestre, F., Rostek, F., Bernasconi, S. M., & Ariztegui, D. (2020). Paleolimnological record of the Pampean plains (Argentina) as a natural archive of South American hydroclimatic variability since the LGM to the Current Warm Period. *Quaternary Science Reviews*, *250*, 106675. https://doi.org/10.1016/j.quascirev.2020.106675

Dearing, J. A., Dann, R. J. L., Hay, K., Lees, J. A., Loveland, P. J., Maher, B. A., & O'Grady, K. (1996). Frequency-dependent susceptibility measurements of environmental materials. *Geophysical Journal International*, *124*(1), 228–240. https://doi.org/10.1111/j.1365-246X.1996.tb06366.x

Delmonte, B., Andersson, P. S., Schöberg, H., Hansson, M., Petit, J. R., Delmas, R., et al. (2010). Geographic provenance of aeolian dust in East Antarctica during Pleistocene glaciations: Preliminary results from Talos Dome and comparison with East Antarctic and new Andean ice core data. *Quaternary Science Reviews*, *29*(1–2), 256–264. https://doi.org/10.1016/j.quascirev.2009.05.010

Delmonte, B., Petit, J. R., Basile-Doelsch, I., Lipenkov, V., & Maggi, V. (2004). First characterization and dating of East Antarctic bedrock inclusions from subglacial Lake Vostok accreted ice. *Environmental Chemistry*, *1*(2), 90–94. https://doi.org/10.1071/EN04029

Dietze, M., Schulte, P., & Dietze, E. (2022). Application of end-member modelling to grain-size data: Constraints and limitations. *Sedimentology*, *69*(2), 845–863. https://doi.org/10.1111/sed.12929

Evans, M. E. (2001). Magnetoclimatology of aeolian sediments. *Geophysical Journal International*, *144*(2), 495–497. https://doi.org/10.1046/j.0956-540X.2000.01317.x

Evans, M. E., & Heller, F. (1994). Magnetic enhancement and palaeoclimate: Study of a loess/palaeosol couplet across the Loess Plateau of China. *Geophysical Journal International*, *117*(1), 257–264. https://doi.org/10.1111/j.1365-246x.1994.tb03316.x

Forster, T., Evans, M. E., & Heller, F. (1994). The frequency dependence of low field susceptibility in loess sediments. *Geophysical Journal International*, *118*(3), 636–642. https://doi.org/10.1111/j.1365-246X.1994.tb03990.x

Gaiero, D. M., Brunet, F., Probst, J. L., & Depetris, P. J. (2007). A uniform isotopic and chemical signature of dust exported from Patagonia: Rock sources and occurrence in southern environments. *Chemical Geology*, *238*(1–2), 107–120. https://doi.org/10.1016/j.chemgeo.2006.11.003

Gaiero, D. M., Simonella, L., Gassó, S., Gili, S., Stein, A. F., Sosa, P., et al. (2013). Ground/satellite observations and atmospheric modeling of dust storms originating in the high Puna-Altiplano deserts (South America): Implications for the interpretation of paleo-climatic archives. *Journal of Geophysical Research: Atmospheres*, *118*(9), 3817–3831. https://doi.org/10.1002/jgrd.50036

Garreaud, R. D., Vuille, M., Compagnucci, R., & Marengo, J. (2009). Present-day South American climate. *Palaeogeography, Palaeoclimatology, Palaeoecology*, *281*(3–4), 180–195. https://doi.org/10.1016/j.palaeo.2007.10.032

Gassó, S., Grassian, V. H., & Miller, R. L. (2010). Interactions between mineral dust, climate, and ocean ecosystems. *Elements*, *6*, 247–252. https://doi.org/10.2113/gselements.6.4.247

Gili, S., Gaiero, D. M., Goldstein, S. L., Chemale, F., Jweda, J., Kaplan, M. R., et al. (2017). Glacial/interglacial changes of Southern Hemisphere wind circulation from the geochemistry of South American dust. *Earth and Planetary Science Letters*, *469*, 98e109. https://doi.org/10.1016/j.epsl.2017.04.007

Ginoux, P., Prospero, J. M., Gill, T. E., Hsu, N. C., & Zhao, M. (2012). Global-scale attribution of anthropogenic and natural dust sources and their emission rates based on MODIS Deep Blue aerosol products. *Reviews of Geophysics*, *50*(3), RG3005. https://doi.org/10.1029/2012RG000388

Gorenstein, I., Prado, L. F., Bianchini, P. R., Wainer, I., Grif, M. L., Pausata, F. S. R., & Yokoyama, E. (2022). A fully calibrated and updated mid-Holocene climate reconstruction for Eastern South America. *Quaternary Science Reviews*, *292*, 107620. https://doi.org/10.1016/j.quascirev.2022.107620

Grousset, F. E., Biscaye, P. E., Revel, M., Petit, J. R., Pye, K., Joussaume, S., & Jouzel, J. (1992). Antarctic (Dome C) icecore dust at 18 ky BP: Isotopic constraints on origins. *Earth and Planetary Science Letters*, *111*(1), 175–182. https://doi.org/10.1016/0012-821X(92)90177-W

Guérin, G., Mercier, N., & Adamiec, G. (2011). Dose-rate conversion factors: Update. *Ancient TL*, *29*, 5e8.

Han, J., Lu, H., Wu, N., & Guo, Z. (1996). The magnetic susceptibility of modern soils in China and its use for paleoclimate reconstruction. *Studia Geophysica et Geodaetica*, *40*, 262–275. https://doi.org/10.1007/bf02300742

Hein, A. S., Cogez, A., Darvill, C. M., Mendelova, M., Kaplan, M. R., Herman, F., et al. (2017). Regional mid-Pleistocene glaciation in central Patagonia. *Quaternary Science Reviews*, *164*, 77–94. https://doi.org/10.1016/j.quascirev.2017.03.023

Heiri, O., Lotter, A. F., & Lemcke, G. (2001). Loss on ignition as a method for estimating organic and carbonate content in sediments: Reproducibility and comparability of results. *Journal of Paleolimnology*, *25*(1), 101–110. https://doi.org/10.1023/A:1008119611481

Heller, F., Shen, C. D., Beer, J., Liu, X. M., Liu, T. S., Bronger, A., et al. (1993). Quantitative estimates and palaeoclimatic implications of pedogenic ferromagnetic mineral formation in Chinese loess. *Earth and Planetary Science Letters*, *114*(2–3), 385–390. https://doi.org/10.1016/0012-821X(93)90038-B

Howard, P. J. A., & Howard, D. M. (1990). Use of organic carbon and loss-on-ignition to estimate soil organic matter in different soil types and horizons. *Biology and Fertility of Soils*, *9*(4), 306–310. https://doi.org/10.1007/bf00634106

Hu, P., Liu, Q., Heslop, D., Roberts, A. P., & Jin, C. (2015). Soil moisture balance and magnetic enhancement in loess–paleosol sequences from the Tibetan Plateau and Chinese Loess Plateau. *Earth and Planetary Science Letters*, *409*, 120–132. https://doi.org/10.1016/j.epsl.2014.10.035

Hu, P., Liu, Q., Torrent, J., Barron, V., & Jin, C. (2013). Characterizing and quantifying iron oxides in Chinese loess/paleosols: Implications for pedogenesis. *Earth and Planetary Science Letters*, *369–370*, 271–283. https://doi.org/10.1016/j.epsl.2013.03.033

Iglesias, V., Whitlock, C., Bianchi, M. M., Villarosa, G., & Outes, V. (2011). Holocene climate variability and environmental history at the Patagonian forest/steppe ecotone: Lago Mosquito (42°29′37.89″S, 71°24′14.57″W) and Laguna del Cóndor (42°20′47.22″S, 71°17′07.62″W). *The Holocene*, *22*(11), 1297–1307. https://doi.org/10.1177/0959683611427330

Iriondo, M. H., & Kröhling, D. M. (2007). Non-classical types of loess. *Sedimentary Geology*, *202*(3), 352–368. https://doi.org/10.1016/j.sedgeo.2007.03.012

Kemp, R. A., Zarate, M., Toms, P., King, M., Sanabria, J., & Argüello, G. L. (2006). Late Quaternary paleosols, stratigraphy and landscape evolution in the Northern Pampa, Argentina. *Quaternary Research*, *66*(1), 119–132. https://doi.org/10.1016/j.yqres.2006.01.001

Koch, P., Wernli, H., & Davies, H. C. (2006). An event-based jet-stream climatology and typology. *International Journal of Climatology*, *26*(3), 283–301. https://doi.org/10.1002/joc.1255

Kohfeld, K. E., Graham, R. M., De Boer, A. M., Sime, L. C., Wolff, E. W., Le Quéré, C., & Bopp, L. (2013). Southern Hemisphere westerly wind changes during the Last Glacial Maximum: Paleo-data synthesis. *Quaternary Science Reviews*, *68*, 76–95. https://doi.org/10.1016/j.quascirev.2013.01.017

Kohfeld, K. E., & Harrison, S. P. (2001). DIRTMAP: The geological record of dust. *Earth-Science Reviews*, *54*(1–3), 81–114. https://doi.org/10.1016/s0012-8252(01)00042-3

Kok, J. F., Parteli, E. J., Michaels, T. I., & Karam, D. B. (2012). The physics of wind-blown sand and dust. *Reports on Progress in Physics*, *75*(10), 106901. https://doi.org/10.1088/0034-4885/75/10/106901

Kruck, W., Helms, F., Geyh, M. A., Suriano, J. M., Marengo, H. G., & Pereyra, F. (2011). Late PleistoceneeHolocene history of Chaco-Pampa sediments in Argentina and Paraguay. *Quaternary Science Journall*, *60*, 188e202.

Lambert, F., Delmonte, B., Petit, J. R., Bigler, M., Kaufmann, P. R., Hutterli, M. A., et al. (2008). Dust-climate couplings over the past 800,000 years from the EPICA Dome C ice core. *Nature*, *452*(7187), 616–619. https://doi.org/10.1038/nature06763

Leger, T. P., Hein, A. S., Bingham, R. G., Rodés, Á., Fabel, D., & Smedley, R. K. (2021). Geomorphology and 10Be chronology of the last glacial maximum and deglaciation in northeastern Patagonia, 43°S–71°W. *Quaternary Science Reviews*, *272*, 107194. https://doi.org/10.1016/j.quascirev.2021.107194

Leger, T. P. M., Hein, A. S., Rodés, Á., Bingham, R. G., Schimmelpfennig, I., Fabel, D., et al. (2023). A cosmogenic nuclide-derived chronology of pre-Last Glacial Cycle glaciations during MIS 8 and MIS 6 in northern Patagonia. *Climate of the Past*, *19*(1), 35–59. https://doi.org/10.5194/cp-19-35-2023

Liu, X., Lu, R., Lü, Z., Du, J., Jia, F., Li, T., et al. (2017). Magnetic susceptibility of surface soils in the Mu Us Desert and its environmental significance. *Aeolian Research*, *28*, 1–12. https://doi.org/10.1016/j.aeolia.2017.07.002

Liu, X., & Mao, X. (2021). Loess-palaeosol sequences in diverse environments: Aeolian accumulation identification and magnetic susceptibility models. *Palaeogeography, Palaeoclimatology, Palaeoecology*, *584*, 110683. https://doi.org/10.1016/j.palaeo.2021.110683

Llano, C. L., de Porras, M. E., Barberena, R., Timpson, A., Beltrame, M. O., & Marsh, E. J. (2020). Human resilience to Holocene climate changes inferred from rodent middens in drylands of northwestern Patagonia (Argentina). *Palaeogeography, Palaeoclimatology, Palaeoecology*, *557*, 109894. https://doi.org/10.1016/j.palaeo.2020.109894

Maher, B. A. (2016). Palaeoclimatic records of the loess/palaeosol sequences of the Chinese Loess Plateau. *Quaternary Science Reviews*, *154*, 23–84. https://doi.org/10.1016/j.quascirev.2016.08.004

Maher, B. A., & Thompson, R. (1995). Paleorainfall reconstructions from pedogenic magnetic susceptibility variations in the Chinese loess and paleosols. *Quaternary Research*, *44*(3), 383–391. https://doi.org/10.1006/qres.1995.1083

Maher, B. Y., & Taylor, R. (1988). Formation of ultra fine-grained magnetite in soils. *Nature*, *336*(6197), 368–379. https://doi.org/10.1038/336368a0

Maher, K. (2011). The role of fluid residence time and topographic scales in determining chemical fluxes from landscapes. *Earth and Planetary Science Letters*, *312*(1–2), 48–58. https://doi.org/10.1016/j.epsl.2011.09.040

Maksic, J., Venancio, I. M., Shimizu, M. H., Chiessi, C. M., Piacsek, P., Sampaio, G., et al. (2022). Brazilian biomes distribution: Past and future. *Palaeogeography, Palaeoclimatology, Palaeoecology*, *585*, 110717. https://doi.org/10.1016/j.palaeo.2021.110717

Martin, L. C. P., Blard, P.-H., Lavé, J., Condom, T., Prémaillon, M., Jomelli, V., et al. (2018). Lake Tauca highstand (Heinrich stadial 1a) driven by a southward shift of the Bolivian high. *Science Advances*, *4*(8), eaar2514. https://doi.org/10.1126/sciadv.aar2514

Martini, M. A., Kaplan, M. R., Strelin, J. A., Astini, R. A., Schaefer, J. M., Caffee, M. W., & Schwartz, R. (2017). Late Pleistocene glacial fluctuations in Cordillera oriental, subtropical Andes. *Quaternary Science Reviews*, *171*, 245–259. https://doi.org/10.1016/j.quascirev.2017.06.033

Marx, S. K., Kamber, B. S., McGowan, H. A., Petherick, L. M., McTainsh, G. H., Stromsoe, N., et al. (2018). Palaeo-dust records: A window to understanding past environments. *Global and Planetary Change*, *165*, 13–43. https://doi.org/10.1016/j.gloplacha.2018.03.001

McGlue, M. M., Cohen, A. S., Ellis, G. S., & Kowler, A. L. (2013). Late Quaternary stratigraphy, sedimentology and geochemistry of an underfilled lake basin in the Puna Plateau (northwest Argentina). *Basin Research*, *25*(6), 638–658. https://doi.org/10.1111/bre.12025

McMillan, M., & Schoenbohm, L. M. (2020). Large-Scale Cenozoic Wind Erosion in the Puna Plateau: The Salina del Fraile Depression. *Journal of Geophysical Research: Earth Surface*, *125*(9), 1–16. https://doi.org/10.1029/2020JF005682

Mendelová, M., Hein, A. S., Rodés, A., & Xu, S. (2020). Extensive mountain glaciation in central Patagonia during Marine Isotope Stage 5. *Quaternary Science Reviews*, *227*, 105996. https://doi.org/10.1016/j.quascirev.2019.105996

Meng, X., Liu, L., Balsam, W., Li, S., He, T., Chen, J., & Ji, J. (2015). Dolomite abundance in Chinese loess deposits: A new proxy of monsoon precipitation intensity. *Geophysical Research Letters*, *42*(23), 10391–10398. https://doi.org/10.1002/2015GL066681

Meng, X., Liu, L., Wang, X. T., Balsam, W., Chen, J., & Ji, J. (2018). Mineralogical evidence of reduced East Asian summer monsoon rainfall on the Chinese loess plateau during the early Pleistocene interglacials. *Earth and Planetary Science Letters*, *486*, 61–69. https://doi.org/10.1016/j.epsl.2017.12.048

Meyers, P. A., & Lallier-vergés, E. (1999). Lacustrine sedimentary organic matter records of late Quaternary paleoclimates. *Journal of Paleolimnology*, *21*(3), 345–372. https://doi.org/10.1023/A:1008073732192

Milana, J. P. (2009). Largest wind ripples on Earth? *Geology*, *37*(4), 343–346. https://doi.org/10.1130/g25382a.1

Milana, J. P., Forman, S., & Kröhling, D. (2010). The largest wind ripples on earth: Reply. *Geology*, *38*(9), e219–e220. https://doi.org/10.1130/G31354Y.1

Milana, J. P., Krohling, D. M., Peralta, C., & Viramonte, J. (2011). New data on the origin of € the unique gravelly aeolian dunes and giant megaripples of the Puna Plateau, Argentina. In *Abstract volume XVIII international INQUA Congress. Bern, Switzerland* (p. 1).

Miller, R. L., Cakmur, R. V., Perlwitz, J., Geogdzhayev, I. V., Ginoux, P., Koch, D., et al. (2006). Mineral dust aerosols in the NASA goddard institute for space sciences ModelE atmospheric general circulation model. *Journal of Geophysical Research*, *111*(D6), D06208. https://doi.org/10.1029/2005jd005796

Mingari, L. A., Collini, E. A., Folch, A., Báez, W., Bustos, E., Osores, M. S., et al. (2017). Numerical simulations of windblown dust over complex terrain: The Fiambalá Basin episode in June 2015. *Atmospheric Chemistry and Physics*, *17*(11), 6759–6778. https://doi.org/10.5194/acp-17-6759-2017

Montecino Jara, D. A., Nogués, V., Cosentino, N. J., Torre, G., Coppo, R., Sawakuchi, A., et al. (2026). Luminescence and paleoenvironmental data from the Lozada loess section, Pampean Plain, Argentina [Dataset]. *Zenodo*. https://doi.org/10.5281/zenodo.18405812

Moreno, P. I., Vilanova, I., Villa-Martínez, R., Dunbar, R. B., Mucciarone, D. A., Kaplan, M. R., et al. (2018). Onset and evolution of southern annular mode-like changes at centennial timescale. *Scientific Reports*, *8*(1), 1–9. https://doi.org/10.1038/s41598-018-21836-6

Munson, S., Belnap, J., & Okin, G. (2011). Responses of wind erosion to climate-induced vegetation changes on the Colorado Plateau. *Proceedings of the National Academy of Sciences of the United States of America*, *108*(10), 3854–3859. https://doi.org/10.1073/pnas.1014947108

Murray, A. S., & Wintle, A. G. (2003). The single aliquot regenerative dose protocol: Potential for improvements in reliability. *Radiation Measurements*, *37*(4–5), 377–381. https://doi.org/10.1016/S1350-4487(03)00053-2

Norte, F. A., Ulke, A. G., Simonelli, S. C., & Viale, M. (2008). The severe zonda wind event of 11 July 2006 east of the Andes Cordillera (Argentine): A case study using the BRAMS model. *Meteorology and Atmospheric Physics*, *102*(1–2), 1–14. https://doi.org/10.1007/s00703-008-0011-6

Orellana, H., Latorre, C., García, J.-L., & Lambert, F. (2023). Spatial analysis of paleoclimate variations based on proxy records in the south-central Andes (18°–35°S) from 32 to 4 ka. *Quaternary Science Reviews*, *313*, 108174. https://doi.org/10.1016/j.quascirev.2023.108174

Orgeira, M. J., & Compagnucci, R. (2006). Correlation between paleosol-soil magnetic signal and climate. *Earth Planets and Space*, *58*(10), 1373–1380. https://doi.org/10.1186/bf03352633

Orgeira, M. J., Egli, R., & Compagnucci, R. H. (2011). A quantitative model of magnetic enhancement in loessic soils. In E. Petrovský, D. Ivers, T. Harinarayana, & E. HerreroBervera (Eds.), *The Earth's magnetic interior, IAGA special Sopron book series book series (IAGA)* (Vol. 1, pp. 361–397). https://doi.org/10.1007/978-94-007-0323-0

Panaiotu, C. G., Panaiotu, E. C., Grama, A., & Necula, C. (2001). Paleoclimatic record from a loess-paleosol profile in Southeastern Romania. *Phys. Chem. Earth A Solid Earth Geodesy*, *26*(11–12), 893–898. https://doi.org/10.1016/S1464-1895(01)00138-7

Paterson, G. A., & Heslop, D. (2015). AnalySize: New software for analyzing and unmixing sediment grain size distribution spectra. In *AGU fall meeting abstracts* (Vol. 2015).EP41B-0933.

Peltier, C., Kaplan, M. R., Sagredo, E. A., Moreno, P. I., Araos, J., Birkel, S. D., et al. (2023). The last two glacial cycles in central Patagonia: A precise record from the Ñirehuao glacier lobe. *Quaternary Science Reviews*, *304*, 107873. https://doi.org/10.1016/j.quascirev.2022.107873

Perić, Z. M., Marković, S. B., Sipos, G., Gavrilov, M. B., Thiel, C., Zeeden, C., & Murray, A. S. (2020). A post-IR IRSL chronology and dust mass accumulation rates of the Nosak loess-palaeosol sequence in northeastern Serbia. *Boreas*, *49*(4), 841–857. https://doi.org/10.1111/bor.12459

Petit, J. R., & Delmonte, B. (2009). A model for large glacial–interglacial climate-induced changes in dust and sea salt concentrations in deep ice cores (central Antarctica): Palaeoclimatic implications and prospects for refining ice core chronologies. *Tellus B: Chemical and Physical Meteorology*, *61*(5), 768–790. https://doi.org/10.1111/j.1600-0889.2009.00437.x

Petit, J. R., Mounier, L., Jouzel, J., Korotkevich, Y. S., & Lorius, C. (1990). Paleoclimatological implications of the Vostok core dust record. *Nature*, *343*(6253), 56–58.

Piovano, E. L., Ariztegui, D., Córdoba, F., Cioccale, M., & Sylvestre, F. (2009). Hydrological Variability in South America Below the Tropic of Capricorn (Pampas and Patagonia, Argentina) during the last 13.0 Ka. In F. Vimeux, F. Sylvestre, & M. Khodri (Eds.), *Past climate variability in South America and surrounding regions. Developments in paleoenvironmental research* (Vol. 14). Springer. https://doi.org/10.1007/978-90-481-2672-9_14

Placzek, C. J., Quade, J., & Patchett, P. J. (2006). Geochronology and stratigraphy of late Pleistocene Lake cycles on the southern Bolivian Altiplano: Implications for causes of tropical climate change. *Geological Society of America Bulletin*, *118*(5–6), 515–532. https://doi.org/10.1130/b25770.1

Placzek, C. J., Quade, J., & Patchett, P. J. (2013). A 130 ka reconstruction of rainfall on the Bolivian Altiplano. *Earth and Planetary Science Letters*, *363*, 97–108. https://doi.org/10.1016/j.epsl.2012.12.017

Porras, M. E., Maldonado, A., Abarzúa, A. M., Cárdenas, M. L., Francois, J. P., MartelCea, A. J., et al. (2012). Postglacial vegetation, fire and climate dynamics at Central Chilean Patagonia (Lake Shaman, 44°S). *Quaternary Science Reviews*, *50*, 71–85.

Prado, L. F., Wainer, I., Chiessi, C. M., Ledru, M.-P., & Turcq, B. (2013). A mid-Holocene climate reconstruction for eastern South America. *Climate of the Past*, *9*(5), 2117–2133. https://doi.org/10.5194/cp-9-2117-2013

Prescott, J. R., & Hutton, J. T. (1994). Cosmic ray contributions to dose rates for luminescence and ESR dating: Large depths and long-term time variations. *Radiation Measurements*, *23*(2–3), 497–500. https://doi.org/10.1016/1350-4487(94)90086-8

Prospero, J. M., Ginoux, P., Torres, O., Nicholson, S. E., & Gill, T. E. (2002). Environmental characterization of global sources of atmospheric soil dust identified with the Nimbus 7 Total Ozone Mapping Spectrometer (TOMS) absorbing aerosol product. *Reviews of Geophysics*, *40*(1), 2-1. https://doi.org/10.1029/2000rg000095

Pye, K., & Tsoar, H. (1987). The mechanics and geological implications of dust transport and deposition in deserts with particular reference to loess formation and dune sand diagenesis in the northern Negev, Israel. *Geological Society, London, Special Publications*, *35*(1), 139–156. https://doi.org/10.1144/GSL.SP.1987.035.01.10

Pye, K., & Zhou, L.-P. (1989). Late Pleistocene and Holocene aeolian dust deposition in north China and the northwest Pacific Ocean. *Palaeogeography, Palaeoclimatology, Palaeoecology*, *73*(1–2), 11–23. https://doi.org/10.1016/0031-0182(89)90041-2

Quade, J., Dente, E., Cartwright, A., Hudson, A. M., Jimenez-Rodriguez, S., & McGee, D. (2022). Central Andean (28–34°S) flood record 0–25 ka from Salinas del Bebedero, Argentina. *Quaternary Research*, *109*, 102–127. https://doi.org/10.1017/qua.2022.1

Quade, J., & Kaplan, M. R. (2017). Lake-level stratigraphy and geochronology revisited at Lago (Lake) Cardiel, Argentina, and changes in the Southern Hemispheric Westerlies over the last 25 ka. *Quaternary Science Reviews*, *177*, 173–188. https://doi.org/10.1016/j.quascirev.2017.10.006

Rojas, M. (2013). Sensitivity of Southern Hemisphere circulation to LGM and 4× CO2 climates. *Geophysical Research Letters*, *40*(5), 965–970. https://doi.org/10.1002/grl.50195

Saxton, K. E., & Rawls, W. J. (2006). Soil water characteristic estimates by texture and organic matter for hydrologic solutions. *Soil Science Society of America Journal*, *70*(5), 1569–1578. https://doi.org/10.2136/sssaj2005.0117

Schaetzl, R. J., Bettis, E. A., Crouvi, O., Fitzsimmons, K. E., Grimley, D. A., Hambach, U., et al. (2018). Approaches and challenges to the study of loess—Introduction to the LoessFest Special Issue. *Quaternary Research*, *89*(3), 563–618. https://doi.org/10.1017/qua.2018.15

Shao, Y. P. (2008). *Physics and modelling ofWind erosion* (2nd ed.). Springer.

Simonsen, M. F., Baccolo, G., Blunier, T., Borunda, A., Delmonte, B., Frei, R., et al. (2019). East Greenland ice core dust record reveals timing of Greenland ice sheet advance and retreat. *Nature Communications*, *10*(1), 4494. https://doi.org/10.1038/s41467-019-12546-2

Song, Y., Shi, Z., Fang, X., Nie, J., Naoto, I., Qiang, X., & Wang, X. (2010). Loess magnetic properties in the III Basin and their correlation with the Chinese Loess Plateau. *Science China Earth Sciences*, *53*(3), 419–431. https://doi.org/10.1007/s11430-010-0011-5

Soteres, R. L., Sagredo, E. A., Kaplan, M. R., Martini, M. A., Moreno, P. I., Reynhout, S. A., et al. (2022). Glacier fluctuations in the northern Patagonian Andes (44S) imply wind-modulated interhemispheric in-phase climate shifts during termination 1. *Scientific Reports*, *12*(1), 1e11. https://doi.org/10.1038/s41598-022-14921-4

Stubbins, B., Leier, A. L., Barbeau, D. L., Pullen, A., Abell, J. T., Nie, J., et al. (2023). Global climate forcing on late Miocene establishment of the Pampean aeolian system in South America. *Nature Communications*, *14*(1), 6899. https://doi.org/10.1038/s41467-023-42537-3

Tchilinguirian, P., & Morales, M. R. (2013). Mid-Holocene paleoenvironments in northwestern Argentina: Main patterns and discrepancies. *Quaternary International*, *307*, 14–23. https://doi.org/10.1016/j.quaint.2012.12.028

Torre, G., Gaiero, D. M., Coppo, R., Cosentino, N. J., Goldstein, S., De Vleeschouwer, F., et al. (2022). Unraveling late Quaternary atmospheric circulation in the Southern Hemisphere through the provenance of Pampean loess. *Earth-Science Reviews*, *232*, 104143. https://doi.org/10.1016/j.earscirev.2022.104143

Torre, G., Gaiero, D. M., Cosentino, N. J., & Coppo, R. (2020). The paleoclimatic message from the polymodal grain-size distribution of late pleistocene-early Holocene Pampean loess (Argentina). *Aeolian Research*, *42*, 100563. https://doi.org/10.1016/j.aeolia.2019.100563

Torre, G., Gaiero, D. M., Sawakuchi, A. O., del Río, I., & Coppo, R. (2019). Revisiting the chronology and environmental conditions for the accretion of late pleistocene-early Holocene Pampean loess (Argentina). *Quaternary Science Reviews*, *213*, 105–119. https://doi.org/10.1016/j.quascirev.2019.04.018

Vandenberghe, J. (2013). Grain size of fine-grained windblown sediment: A powerful proxy for process identification. *Earth-Science Reviews*, *121*, 18–30. https://doi.org/10.1016/j.earscirev.2013.03.001

Vera, C., Silvestri, G., Liebmann, B., & González, P. (2006). Climate change scenarios for seasonal precipitation in South America from IPCC-AR4 models. *Geophysical Research Letters*, *33*(13). https://doi.org/10.1029/2006GL025759

Villarreal, M. L., & Coronato, A. (2017). Characteristics and nature of pans in the semiarid temperate-cold steppe of Tierra del Fuego. In E. J. Rabassa (Ed.), *Advances in geomorphology and Quaternary studies in Argentina* (pp. 203–224). Springer.

Wainer, I., Ledru, M. P., Clauzet, G., Otto-Bliesner, B., & Brady, E. (2005). Last Glacial Maximum in South America: Paleoclimate proxies and model results. *Geophysical Research Letters*, *32*(16), L16707. https://doi.org/10.1029/2004GL021244

Whitlock, C., Bianchi, M. M., Bartlein, P. J., Markgraf, V., Marlon, J., Walsh, M., & McCoy, N. (2006). Postglacial vegetation, climate, and fire history along the east side of the Andes (lat 41–42.5° S), Argentina. *Quaternary Research*, *66*(2), 187–201. https://doi.org/10.1016/j.yqres.2006.04.004

Woodward, S. (2001). Modeling the atmospheric life cycle and radiative impact of mineral dust in the Hadley Centre climate model. *Journal of Geophysical Research*, *106*(D16), 18155–18166. https://doi.org/10.1029/2000JD900795

Yi, S., Buylaert, J. P., Murray, A. S., Thiel, C., Zeng, L., & Lu, H. (2015). High resolution OSL and post-IR IRSL dating of the last interglacial–glacial cycle at the Sanbahuo loess site (northeastern China). *Quaternary Geochronology*, *30*, 200–206. https://doi.org/10.1016/j.quageo.2015.02.013

Zamanian, K., Pustovoytov, K., & Kuzyakov, Y. (2016). Pedogenic carbonates: Forms and formation processes. *Earth-Science Reviews*, *157*, 1–17. https://doi.org/10.1016/j.earscirev.2016.03.003

Zan, J., Fang, X., Nie, J., Teng, X., & Yang, S. (2012). Rock magnetism in loess from the middle Tian Shan: Implications for paleoenvironmental interpretations of magnetic properties of loess deposits in Central Asia. *Geochemistry, Geophysics, Geosystems*, *13*(10), Q10Z50. https://doi.org/10.1029/2012GC004251

Zan, J., Fang, X., Yang, S., Nie, J., & Li, X. (2010). A rock magnetic study of loess from the West Kunlun Mountains. *Journal of Geophysical Research*, *115*(B10), B10101. https://doi.org/10.1029/2009JB007184

Zárate, M. (2003). Loess of southern South America (Vol. *22*, pp. 1987–2006).

Zech, J., Terrizzano, C. M., García Morabito, E., Veit, H., & Zech, R. (2017). Timing and extent of late Pleistocene glaciation in the arid Central Andes of Argentina and Chile (22°–41°S). *Geogr. Res. Lett.*, *43*, 697–718. https://doi.org/10.18172/cig.3235

Zech, R., May, J.-H., Kull, C., Ilgner, J., Kubik, P. W., & Veit, H. (2008). Timing of the late Quaternary glaciation in the Andes from ∼15 to 40 S. *Journal of Quaternary Science*, *23*(6–7), 635–647. https://doi.org/10.1002/jqs.1200

Zeeden, C., Dietze, M., & Kreutzer, S. (2018). Discriminating luminescence age uncertainty composition for a robust Bayesian modelling. *Quaternary Geochronology*, *43*, 30–39. https://doi.org/10.1016/j.quageo.2017.10.001

Zeeden, C., Hambach, U., Veres, D., Fitzsimmons, K., Obreht, I., Bosken, J., & Lehmkuhl, F. (2018). Millennial scale climate oscillations recorded in the lower Danube loess over the last glacial period. *Palaeogeography, Palaeoclimatology, Palaeoecology*, *509*, 164–181. https://doi.org/10.1016/j.palaeo.2016.12.029

Zeeden, C., Kels, H., Hambach, U., Schulte, P., Protze, J., Eckmeier, E., et al. (2016). Three climatic cycles recorded in a loess-palaeosol sequence at Semlac (Romania)—Implications for dust accumulation in South-Eastern Europe. *Quaternary Science Reviews*, *154*, 130–142. https://doi.org/10.1016/j.quascirev.2016.11.002

Zender, C. S., Bian, H., & Newman, D. (2003). Mineral dust entrainment and deposition (DEAD) model: Description and 1990s dust climatology. *Journal of Geophysical Research*, *108*(D14), 4416. https://doi.org/10.1029/2002JD002775

Zhang, X. Y., Arimoto, R., & An, Z. S. (1997). Dust emission from Chinese desert sources linked to variations in atmospheric circulation. *Journal of Geophysical Research*, *102*(D23), 28041–28047. https://doi.org/10.1029/97jd02300

Zhang, Z., Zheng, Z., Meng, X., Lai, Z., Hou, Y., & Ji, J. (2023). Gradually increasing precipitation since 20 ka as evidenced by loess dolomite abundance in the III Basin, Central Asia. *Catena*, *232*, 107420. https://doi.org/10.1016/j.catena.2023.107420